
Deep Learning on Implicit Neural Datasets

Clinton J. Wang
MIT CSAIL
clintonw@csail.mit.edu

Polina Golland
MIT CSAIL
polina@csail.mit.edu

Abstract

Implicit neural representations (INRs) have become fast, lightweight tools for storing continuous data, but to date there is no general method for learning directly with INRs as a data representation. We introduce a principled deep learning framework for learning and inference directly with INRs of any type without reverting to grid-based features or operations. Our INR-Nets evaluate INRs on a low discrepancy sequence, enabling quasi-Monte Carlo (QMC) integration throughout the network. We prove INR-Nets are *universal approximators* on a large class of maps between L^2 functions. Additionally, INR-Nets have convergent gradients under the empirical measure, enabling backpropagation. We design INR-Nets as a continuous generalization of discrete networks, enabling them to be initialized with pre-trained models. We demonstrate learning of INR-Nets on classification (INR \rightarrow label) and segmentation (INR \rightarrow INR) tasks.

1 Introduction

Implicit neural representations (INRs), which encode signals as the parameters of a neural network, have a number of useful properties. INRs can store continuous data in a memory-efficient manner [37], represent and render detailed 3D scenes at lightning speeds [27], and integrate data from a wide range of modalities [17]. INRs are thus an appealing data representation for many applications, and recently methods for storing data as INRs have been demonstrated [12, 16].

However, no general framework for learning from a collection of data captured as INRs exists today. Converting such an implicit neural dataset into pixels or voxels and applying existing discrete models compounds interpolation errors and sacrifices many desirable properties of INRs [12, 35]. Alternatively, a hypernetwork can be trained in the parameter space of INRs and tailored for downstream tasks [12, 40]. Unfortunately, a hypernetwork based on the parameter space of one type of INR is incompatible with other types, which poses a problem since the parameterization of INRs is constantly evolving. Moreover, these methods are unsuitable for important classes of INRs whose parameters extend beyond a neural network, such as plenoxels [2] and Instant NGPs [27].

In this paper we propose the *INR-Net*, a deep learning framework that directly handles INRs as input or output (Fig. 1). An INR-Net consists of a sequence of layers that compute integrals over parametric functions of the input INR, separated by pointwise nonlinearities. By sampling from a low discrepancy point sequence, these integrals can be estimated efficiently with the quasi-Monte Carlo (QMC) method. INR-Nets generalize standard neural networks including convolutional neural networks and transformers from data on a grid to data on arbitrary manifolds. Thus INR-Nets are a broad class of models that can be applied to classification, segmentation, generative modeling, and other tasks on INRs.

Furthermore, INR-Nets can be applied to any type of INR, or in fact any data that can be represented as integrable functions on a bounded measurable set. Because INR-Nets can evaluate an INR on an arbitrary number of points, they flexibly trade off speed and accuracy, and we find that they generalize

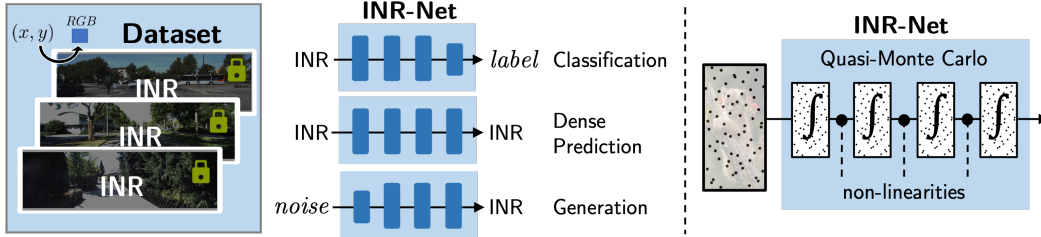


Figure 1: **INR-Nets learn directly from datasets of implicit neural representations (INRs).** The INR-Net processes an INR by evaluating it on a low discrepancy point set, which is used to perform quasi-Monte Carlo integration throughout the network. By treating the frozen INR as a black box, we are not constrained by any particular type of INR, and need not be involved in the INR training process. This framework can be used for a broad range of tasks including classification, dense prediction, and generative modeling.

to varying data resolutions. By constructing layers analogously to discrete networks, INR-Nets can be initialized from a pre-trained discrete network, then fine-tuned with a small INR dataset.

Our contributions are as follows:

- We introduce the INR-Net, the first general framework for learning from implicit neural datasets of arbitrary parameterization.
- We prove desirable properties of the INR-Net. Specifically, INR-Nets are universal approximators, convergent under empirical backpropagation, and can match the behavior of a wide class of discrete models.
- We show that the INR-Net can be initialized from a pre-trained discrete network and analyze its performance under different sampling schemes.
- We demonstrate INR-Nets on classification and segmentation of INRs.

2 Related Work

Implicit neural representations Previous work showed that multilayer perceptrons (MLPs) can be trained to capture a wide range of continuous data with high fidelity. The most prominent domains include shapes [25, 32], objects [28, 31], and 3D scenes [26, 38]. Example applications also extend to gigapixel images [24], volumetric medical images [9], acoustic data [16, 37], tactile data [17], depth and segmentation maps [19], and 3D motion [30]. Additionally, MLPs have been used to generate a continuous volumetric feature field in the middle of a neural network [29, 35]. Such a feature field acts as an implicit representation of an object’s features, and permits latent space manipulations such as changing the object’s appearance and shape. Hypernetwork-based methods for efficiently generating new INRs from sparse data or from noise have been demonstrated in many applications [35–38, 40], and often rely on meta-learning.

Datasets of INRs The idea of storing implicit representations of objects to form a dataset has been previously presented as a way of integrating disparate modalities into a single data format [16, 17]. Others present the case for creating datasets of INRs to efficiently meta-learn hypernetworks for various tasks [11, 12] including generative modeling, data imputation, novel view synthesis and classification.

Approximation capabilities of neural networks A fundamental result in approximation theory is that the set of single-layer neural networks is dense in a large space of functionals, namely $L^p(\mu)$ for all finite measures μ on \mathbb{R}^n as well as $\mathcal{C}(X)$ for all compact subsets X of \mathbb{R}^n [18]. Subsequent works designed constructive examples using various non-linear activations [6, 7]. While this result is readily extended to multi-dimensional outputs, to the best of our knowledge, no approximation results for the case of infinite dimensional outputs (e.g., $L^p(\mu) \rightarrow L^p(\mu)$) exists today, nor is there analysis examining universal approximation in the context of networks that incorporate numerical integration.

Continuous convolutions The continuous convolution operator has an extensive history, and its applications in deep learning has appeared in many contexts including modeling point clouds [3, 43], graphs [15], fluids [42], and sequential data [33, 34]. It is invaluable for processing irregularly sampled data while maintaining translation invariance and locality. These properties make the continuous convolution an ideal core layer for INR-Net architectures.

3 Principles of INR-Nets

In this section we provide a definition of an INR-Net, then derive three important properties that enable INR-Nets to serve as a general deep learning framework. Specifically, INR-Nets are agnostic to INR parameterization, are universal approximators, and exhibit convergent empirical gradients.

3.1 Preliminaries and Foundational Layers

Let Ω be a bounded measurable subset of a d -dimensional compact metric space. The most common case is $\Omega \subset \mathbb{R}^d$, and in the Appendix we consider the case of a d -dimensional manifold. Let \mathcal{F}_c denote the space $L^2(\Omega, \mathbb{R}^c) = \{f : \Omega \rightarrow \mathbb{R}^c : \int_{\Omega} \|f\|^2 d\mu < \infty\}$. We refer to all maps $f \in \mathcal{F}_c$ as INRs, although such maps also encompass many other types of signals and data formats. We call d the *dimensionality* of the INR (e.g., 2 for SIREN [37], 3 for occupancy networks [25], 5 for NeRF [26]) and c the number of *channels* of the INR (e.g., 3 for SIREN, 1 for occupancy networks, 4 for NeRF).

An INR-Net layer \mathcal{H} is a bounded continuous map $\mathcal{F}_n \rightarrow \mathcal{F}_m$ (e.g., linear combinations of channels), or $\mathbb{R}^n \rightarrow \mathcal{F}_m$ (e.g., in a generator), or $\mathcal{F}_n \rightarrow \mathbb{R}^m$ (e.g., in a classifier), or $\mathcal{F}_n \times \mathcal{F}_m \rightarrow \mathcal{F}_c$ (e.g., in style transfer) for some $n, m, c \in \mathbb{N}$. An INR-Net is a directed acyclic graph of network layers¹. Many loss functions and regularizers on images and other spatial data generalize naturally to the continuous domain as bounded continuous maps $\mathcal{F}_c \rightarrow \mathbb{R}$ or $\mathcal{F}_c \times \mathcal{F}_c \rightarrow \mathbb{R}$. Our definition of the INR-Net implies the following property:

Property 1 (INR-Parameterization Agnostic) *An INR-Net is agnostic to the parameterization of the data used to train it. If $f, g \in \mathcal{F}_c$ are equal in the sense that $f_i = g_i$ for all $i \in \{1, \dots, c\}$, then any INR-Net or loss function on \mathcal{F}_c maps f and g to the same output.*

For simplicity we characterize the single-channel layers, i.e., the bounded continuous maps $L^2(\Omega) \rightarrow L^2(\Omega)$, $L^2(\Omega) \rightarrow \mathbb{R}^n$, and $\mathbb{R}^n \rightarrow L^2(\Omega)$. In Appendix B we extend each of our results to the multi-channel case. Let us stipulate that an INR-Net layer $\mathcal{H}_{\phi} : L^2(\Omega) \rightarrow \mathbb{R}^n$ can be expressed as:

$$\mathcal{H}_{\phi}[f] = \int_{\Omega} H_{\phi}[f](x) dx \quad (1)$$

$$= \int_{\Omega} h(x, f(x), \dots, D^{\alpha} f(x); \phi) dx, \quad (2)$$

for a function h which is Fréchet differentiable at all $f \in L^2(\Omega)$, is of bounded variation² in Ω for all f , is differentiable w.r.t. its parameters ϕ , and has weak derivative $D^{\alpha} f = \frac{\partial^{|\alpha|} f}{\partial x_1^{\alpha_1} \dots \partial x_n^{\alpha_n}}$ for multi-index α . The dependence of h on weak derivatives up to order $k = |\alpha|$ requires that the weak derivatives are integrable, i.e., f is in the Sobolev space $W^{k,2}(\Omega)$. Similarly, an INR-Net layer $\bar{\mathcal{H}}_{\phi'} : L^2(\Omega) \rightarrow L^2(\Omega)$ can be expressed as:

$$\bar{\mathcal{H}}_{\phi'}[f](x') = \int_{\Omega} \bar{h}(x, f(x), \dots, D^{\alpha} f(x), x', f(x'), \dots, D^{\alpha} f(x'); \phi') dx, \quad (3)$$

A minimal set of layers Each INR channel $f \in L^2(\Omega)$ is automatically endowed with addition, pointwise multiplication, the norms $\|f\|_p = (\int_{\Omega} |f|^p d\mu)^{1/p}$ for $p \in [1, 2]$, and the inner product $\langle f, g \rangle = \int_{\Omega} fg d\mu$, which can be freely used in an INR-Net or its loss functions. For a map $\mathbb{R}^n \rightarrow L^2(\Omega)$, consider the bounded linear map that takes as input n numbers and treats them

¹INR-Nets can include both INR-Net layers as well as classical neural network layers that are bounded continuous maps $\mathbb{R}^n \rightarrow \mathbb{R}^m$.

²See Appendix A for details on how we characterize the variation of a function.

as coefficients of an orthonormal polynomial basis on Ω . To generate non-linearities we add a class of layers defined by a pointwise transformation. A locally bounded piecewise continuous non-polynomial [20] function $\sigma : \mathbb{R} \rightarrow \mathbb{R}$ defines the activation layer $\mathcal{H} : L^2(\Omega) \rightarrow L^2(\Omega)$ such that $\mathcal{H}[f](x) = \sigma(f(x))$ for all $x \in \Omega$. Layers based on these operations alone grant us a fully expressive space of networks, as we can learn arbitrary connections between different parts of Ω by polynomials of sufficient order, and perform nonlinear combinations of their values.

3.2 Numerical Integration

By eqn. (1) and (3), every non-pointwise layer involves integrating over Ω , and the integrand will rarely have an analytic form. Quasi-Monte Carlo (QMC) offers a fast method for estimating such integrals with favorable convergence rates compared to standard Monte Carlo [5]. QMC generates a low discrepancy³ sequence of points on Ω , which can be reused for the entire network as long as layers preserve the domain Ω . The sequence can be deterministic or pseudorandom as needed.

At inference time, INR-Net has the option to trade off speed to obtain some desired error bounds with adaptive quadrature techniques⁴, which can be valuable in applications requiring robustness or verifiability. For general applications it is more convenient to use QMC as it only requires a single pass through the network, and enables the same point set to be used for all INRs in a minibatch (we can still randomize between minibatches).

With a method for estimating the output of each layer to arbitrary accuracy, we are now ready to state the second key property of INR-Nets:

Property 2 (Universal Approximator) *Let $\mathcal{G}, \mathcal{G}'$ be subsets on $L^2(\Omega)$ restricted to piecewise smooth functions, with mild conditions on Ω . For every Lipschitz continuous map $\mathcal{R} : \mathcal{G} \rightarrow \mathcal{G}'$, there exists an INR-Net \mathcal{T} that approximates it to arbitrary accuracy w.r.t. a finite measure ν on \mathcal{G} . As a corollary, every Lipschitz continuous map $\mathcal{G} \rightarrow \mathbb{R}^n$ or $\mathbb{R}^n \rightarrow \mathcal{G}$ can also be approximated by some INR-Net.*

Appendix B.1 provides a full proof, including the extension to multi-channel maps. A high-level sketch of the $\mathcal{G} \rightarrow \mathcal{G}'$ case is as follows:

1. Fix a low discrepancy sequence of points $\{x_j\}_{j=1}^N$ in Ω that can approximate any function in $\mathcal{G} \cup \mathcal{G}'$ with QMC to desired accuracy.
2. Let π be the projection of a function $f \in \mathcal{G} \cup \mathcal{G}'$ to \mathbb{R}^N by selecting its N values at the QMC sample points. Through π , the measure ν on \mathcal{G} induces a measure μ on \mathbb{R}^N .
3. We can construct an MLP that approximates any function in $L^2(\mathbb{R}^N)$, by covering the volume under the graph of the function with rectangles, and then at inference time summing the rectangles under the given \mathbb{R}^N input [23]. Here, we cover the graph of $(\pi f, \mathcal{R}[f](x_j))$ for each QMC sample point x_j , and compute volumes w.r.t. μ . The INR-Net specifies the desired connections on Ω using element-wise products with cutoff functions and linear combinations of channels.
4. Repeating this construction N times, we fully specify the desired behavior of $f \mapsto \mathcal{R}[f]$ to desired accuracy w.r.t. the measure ν .

3.3 Backpropagation

Although QMC is guaranteed to converge to the correct integrals in forward passes through an INR-Net, we need to verify that differentiation through the empirical measure converges to the appropriate derivatives. In particular, we demonstrate the following property:

Property 3 (Convergent Empirical Gradients) *An INR-Net permits backpropagation of its outputs with respect to its input as well as all its learnable parameters. Within each layer, the gradients*

³The discrepancy of a point set measures how well-distributed it is on a domain. When a function is evaluated on a point set, the discrepancy tightly bounds the error of the sample mean as an estimate of the function’s integral over the domain. Examples of low discrepancy sequences include the Halton and Sobol sequences, and notably exclude regular grids. See Appendix A for more information on QMC and low discrepancy sequences.

⁴In general, the error bounds are only tight for functions in $\mathcal{C}^1([a, b]^d)$ [13]. An adaptive integration scheme such as Gauss-Kronrod quadrature repeatedly evaluates the integrand at finer scales where the curvature is greatest until the desired accuracy is achieved.

along a low discrepancy sequence in Ω , if they exist, converge to the appropriate derivative under the measure on Ω .

This property is proved in full in Appendix B.2. Here we briefly describe the case for a single-channel layer $\mathcal{H}_\phi : L^2(\Omega) \rightarrow \mathbb{R}$ requiring QMC integration. Choose a family of sequences $\{X_N\}_{N \in \mathbb{N}} : X_N = \{x_j\}_{j=1}^N$ on Ω whose discrepancy converges to 0 as $N \rightarrow \infty$.

Gradients w.r.t. parameters: We claim that the empirical gradient of $\mathcal{H}_\phi[f]$ w.r.t. ϕ converges in N for all $f \in L^2(\Omega)$. For each parameter ϕ_k ,

$$\lim_{N \rightarrow \infty} \frac{\partial}{\partial \phi_k} \left(\frac{1}{N} \sum_{j=1}^N H_\phi[f](x_j) \right) = \frac{\partial}{\partial \phi_k} \mathcal{H}_\phi[f], \quad (4)$$

where H_ϕ is the integrand from eqn. (1). Thus the limit of the empirical gradient is simply the set of partial derivatives of \mathcal{H}_ϕ w.r.t. each parameter.

Gradients w.r.t. inputs: For fixed $\tilde{x} \in \Omega$, the empirical derivative of \mathcal{H}_ϕ w.r.t. $f(\tilde{x})$ converges uniformly in N . In particular, we can design a sequence of bump functions $\{\psi_{\tilde{x}, N}\}_{N \in \mathbb{N}}$ which is 1 in a small neighborhood around \tilde{x} and vanishes at each $x_j \neq \tilde{x}$, such that:

$$\lim_{N \rightarrow \infty} \frac{\partial}{\partial f(\tilde{x})} \left(\frac{1}{N} \sum_{j=1}^N H_\phi[f](x_j) \right) = \lim_{N \rightarrow \infty} \nabla_{\psi_{\tilde{x}, N}} \mathcal{H}_\phi[f]. \quad (5)$$

So the empirical derivative converges to the limit of the directional derivatives of $\mathcal{H}_\phi[f]$ w.r.t. a decreasing sequence of bump functions at \tilde{x} , which is finite due to Fréchet differentiability of H_ϕ .

In Appendix B.2 we show these results naturally extend to the vector-valued case $L^2(\Omega) \rightarrow \mathbb{R}^n$ and INR-valued case $L^2(\Omega) \rightarrow L^2(\Omega)$ via the Gateaux derivative. Using the chain rule for Gateaux derivatives, we also show that the empirical gradients through multiple layers converge to the chained Gateaux derivatives. Therefore backpropagation through the entire INR-Net is convergent.

4 Design and Implementation of INR-Nets

4.1 INR-Nets as Generalizations of Discrete Models

A natural starting point for designing INR-Nets is to mimic the architectures used for discrete networks. For example, consider an RGB image as a map $\tilde{f} : \tilde{\Omega} \rightarrow \mathbb{R}^3$ for pixel coordinates $\tilde{\Omega} \subset \mathbb{Z}^2$. An ideal INR of the same image learns a map $f : \Omega \rightarrow \mathbb{R}^3$ for coordinates $\Omega \subset \mathbb{R}^2$ such that $\tilde{f} = f|_{\tilde{\Omega}}$. For any image classification network $\tilde{\mathcal{T}}_\psi : \tilde{f} \rightarrow [0, \dots, N_{\text{cls}}]$, we can create an equivalent INR classifier $\mathcal{T}_\theta : f \rightarrow [0, \dots, N_{\text{cls}}]$ by replacing each layer that operates on pixels $\tilde{\Omega}$ with a layer that operates on continuous coordinates Ω , replacing summations over pixel values with integrals.

Indeed, we can design networks that are not only architecturally equivalent, but also functionally equivalent in the following sense:

Property 4 (Equivalence to Discrete Networks) *Every discrete network layer that operates on $\ell^2(\tilde{\Omega})$ for some $\tilde{\Omega} \subset \Omega$ can be transformed into an INR-Net layer on $L^2(\Omega)$ that reproduces its behavior exactly when restricted to samples from $\tilde{\Omega}$. By transforming each layer of a pre-trained discrete network in this manner, the resultant INR-Net can reproduce the behavior of the discrete network as a whole.*

For our image classifier example, this means there is a straightforward algorithm for parameter conversion $\theta = \text{convert}(\psi)$ for which $\tilde{f} = f|_{\tilde{\Omega}}$ implies $\tilde{\mathcal{T}}_\psi(\tilde{f}) = \mathcal{T}_\theta(f; \tilde{\Omega})$, i.e., all matching pairs of images and INRs produce the same class predictions when integrals in \mathcal{T}_θ are approximated using the same grid points as the discrete network.

We design a set of INR-Net layers that replicate discrete layers in this sense, including normalization, max pooling, tokenization and attention. We describe convolutional layers and multi-scale architectures here (also see Fig. 2) and describe other layers and blocks in Appendix C.

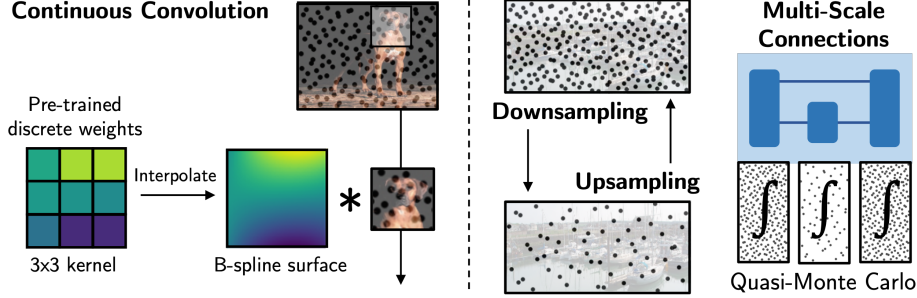


Figure 2: **INR-Nets are continuous analogues of a large class of discrete networks.** INR-Net layers generalize operations on grids to a continuous domain, suitable for quasi-Monte Carlo integration. Low discrepancy point sets are amenable to the multi-scale structures often found in discrete networks. INR-Nets composed of these layers can be initialized from pre-trained discrete networks including convolutional neural networks and vision transformers.

Convolution For a measurable $S \subset \Omega$ and a polynomial basis $\{p_{j,\phi}\}_{j \geq 0}$ that spans $L^2(S)$, we call S the support of a polynomial convolutional kernel $K_\phi : \Omega \times \Omega \rightarrow \mathbb{R}$ defined by:

$$K_\phi(\mathbf{x}, \mathbf{x}') = \begin{cases} \sum_{j=0}^n p_{j,\phi}(\mathbf{x} - \mathbf{x}')^j & \text{if } \mathbf{x} - \mathbf{x}' \in S \\ 0 & \text{otherwise.} \end{cases} \quad (6)$$

for some chosen $n \in \mathbb{N}$. A convolution is the linear map $\mathcal{H}_\phi : L^2(\Omega) \rightarrow L^2(\Omega)$ given by:

$$\mathcal{H}_\phi[f] = \int_{\Omega} K_\phi(\cdot, \mathbf{x}') f(\mathbf{x}') d\mathbf{x}'. \quad (7)$$

To transfer weights from a discrete convolution, K_ϕ can be parameterized as a rectangular B-spline surface that interpolates the weights (Fig. 2 left).

An MLP convolution is defined similarly except the kernel becomes $\tilde{K}_\phi(\mathbf{x}, \mathbf{x}') = \text{MLP}(\mathbf{x} - \mathbf{x}'; \phi)$ in the non-zero case. While MLP kernels are favored over polynomial kernels in many applications due to their expressive power [43], MLP kernels cannot be initialized with discrete convolutional weights. Moreover, polynomial bases can be used to construct filters satisfying desired properties such as equivariance, k -Lipschitz continuity, or boundary conditions.

Multi-scale architectures Under QMC, downsampling is easily implemented by truncating the list of coordinates in the low-discrepancy sequence to the desired number of terms, as the truncated sequence is itself low-discrepancy. Similarly, upsampling is implemented by extending the low-discrepancy sequence to the desired number of terms, then performing nearest neighbor interpolation. Although other types of interpolation on rectilinear grids do not translate directly to a collection of points, we can replicate their behavior at fixed scale using an appropriately designed convolution filter. Since downsampling and upsampling are both specified with respect to the same low-discrepancy sequence, INR-Nets can use multi-scale structures with residual or skip connections (Fig. 2 right).

Using pre-trained discrete models as a starting point to refine INR-Nets alleviates the need for large INR datasets as the network can simply be fine-tuned. Further investigation is required to find stable ways to leverage this equivalence, as we discuss in Section 6.

4.2 Training INR-Nets

As with discrete networks, the pipelines for training INR-Nets vary with the task. We outline steps for training a classifier, dense prediction model, and unconditional generator in Algorithms 1, 2 and 3. Similar pipelines can be used to train models for other tasks on INRs such as scene editing, inverse problems, or representation learning.

An INR classifier is trained similarly to a discrete network, except that query points for QMC integration must be specified to generate the output logits. In contrast, networks for dense prediction or generative modeling produce an INR without specifying where it will be evaluated. Evaluating the output INR at particular coordinates then invokes the appropriate evaluations of the input INR (if

Table 1: INR classifier top-3 accuracy at two resolutions (ImageNet-Big12 [14]).

Model Type	32 × 32	64 × 64
2-layer CNN	59.8%	54.1%
INR-Net-2 (ours)	56.6%	55.2%
4-layer CNN	65.7%	53.5%
INR-Net-4 (ours)	57.4%	56.4%

Table 2: INR segmentation performance (Cityscapes [8]).

Model Type	Coarse Segs		Fine Segs	
	mIoU	PixAcc	mIoU	PixAcc
3-layer FCN	0.409	69.6%	0.374	63.6%
INR-Net-3 (ours)	0.471	78.5%	0.417	69.4%
5-layer FCN	0.488	79.4%	0.436	72.5%
INR-Net-5 (ours)	0.443	77.7%	0.394	68.4%

applicable) and subsequent network computations. The output INR is parameterized by the input INR and the INR-Net, as it has no separate parameters of its own.

Algorithm 1 Training for Classification

Input: network \mathcal{T}_θ , INR/label dataset \mathcal{D}
 Choose classifier loss \mathcal{L} , number of INR evaluations N , low-discrepancy sampler LD
for step $s \in 1 : N_{\text{steps}}$ **do**
 INRs f_i , labels $y_i \leftarrow \text{minibatch}(\mathcal{D})$
 Query points $\mathbf{x} \leftarrow LD(N)$
 Label estimates $\hat{y}_i \leftarrow \mathcal{T}_\theta(f_i; \mathbf{x})$
 Backpropagate $\mathcal{L}(\hat{y}_i, y_i)$ to update θ
end
Output: trained network \mathcal{T}_θ

Algorithm 2 Training for Dense Prediction

Input: network \mathcal{T}_θ , INR/label dataset \mathcal{D} with dense coordinate-label pairs
 Choose task-specific loss \mathcal{L}
for step $s \in 1 : N_{\text{steps}}$ **do**
 INRs f_i , point labels $(\mathbf{x}_{ij}, y_{ij}) \leftarrow \text{minibatch}(\mathcal{D})$
 Output INRs $g_i \leftarrow \mathcal{T}_\theta[f_i]$
 Point label estimates $\hat{y}_{ij} \leftarrow g_i(\mathbf{x}_{ij})$
 Backpropagate $\mathcal{L}(\hat{y}_{ij}, y_{ij})$ to update θ
end
Output: trained network \mathcal{T}_θ

4.3 Computational Complexity

The INR-Net’s complexity is similar to that of a discrete model with an equivalent architecture. In general time and memory both scale linearly with the number of sample points (regardless of the dimensionality of Ω), as well as with network depth and width.

Implemented naively, the computational cost of the continuous convolution is quadratic in the number of sample points, as it must calculate weights separately for each neighboring pair of points. We can reduce this to a linear cost by specifying a N_{bin} Voronoi partition of the kernel support B , then using the value of the kernel at each seed point for all points in its cell. Thus the kernel need only be evaluated N_{bin} times regardless of the number of sample points. Additionally N_{bin} can be modified during training and inference.

Algorithm 3 Training Unconditional Generator

Input: network \mathcal{T}_θ , INR dataset \mathcal{D}
 Choose model-specific loss \mathcal{L} , number of INR evaluations N , low-discrepancy sampler LD
for step $s \in 1 : N_{\text{steps}}$ **do**
 INRs $f_i \leftarrow \text{minibatch}(\mathcal{D})$
 Noise $z_j \leftarrow \mathcal{N}(\mathbf{0}, \mathbf{I})$
 Generated INRs $g_j \leftarrow \mathcal{T}_\theta[z_j]$
 Query points $\mathbf{x} \leftarrow LD(N)$
 Backpropagate $\mathcal{L}(f_i, g_j; \mathbf{x})$ to update θ
end
Output: trained network \mathcal{T}_θ

5 Experiments

We demonstrate our framework on classifying and segmenting INRs fit to natural images. Our aim is not to compete with pixel-based methods on each task, but rather to demonstrate that the INR-Net offers a feasible framework for performing inference on implicit neural datasets. Appendix D provides further details on each dataset used in our experiments.

5.1 INR Classification

We perform classification on a dataset of 8,400 INRs fit to natural images. We use a subset of ImageNet1k [10] with 700 samples from each of 12 superclasses [14]. For each class we train on 500 SIRENs [37] and evaluate on 200 Gaussian Fourier feature networks [41]. We analyze the differences between these INR parameterizations in Appendix D.1.

We train INR-Nets with 2 and 4 MLP convolutional layers (INR-Net-2 and INR-Net-4), as well as architecturally equivalent convolutional neural networks (CNNs). Each network is trained for 8K iterations with an AdamW optimizer [22] and a learning rate of 10^{-3} . INR-Net-4 performs a forward pass on a batch of 48 images in 96 ± 4 ms on a single NVIDIA RTX 2080 Ti GPU. The CNNs sample

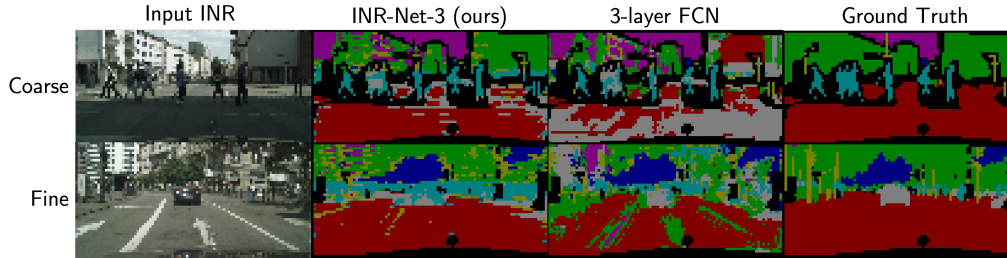


Figure 3: Cityscapes INR segmentations for models trained on coarse segs only. INR-Net produces INR segmentations, which can be evaluated at the subpixel level.

INRs along the 32×32 grid while INR-Nets generate 1024 points from a scrambled Sobol sequence. We evaluate with top-3 accuracy at the same resolution as well as at higher resolution (64×64 or 4096 points).

INR-Nets somewhat underperform their CNN counterparts (Table 1), and the gap in performance is larger for the deeper models. However, they generalize better to higher-resolution images, outperforming the CNNs on images at twice the resolution, with a very small drop in performance. We hypothesize that INR-Nets maintain stable behavior under such shift because the support of the continuous convolution kernel remains fixed in size, while the discrete convolution shrinks its receptive field relative to the size of the image as the resolution increases. Thus the distribution of features may be more consistent in INR-Net layers, pointing to an interesting future direction for optimizing INR-Net performance.

5.2 Semantic Segmentation of an INR

We perform pixel-wise segmentation on SIRENs fit to street view images from Cityscapes [8], grouping the segmentation labels into 7 categories. We train on 2975 INRs with coarsely annotated segmentations only, and test on 500 INRs with both coarse and fine annotations (Fig. 3). Discrete models sample the 48×96 grid, and the INR-Nets sample 4608 points. We compare the performance of 3 and 5 layer INR-Nets and fully convolutional networks (FCNs). Networks are trained for 10K iterations with a learning rate of 10^{-3} . We evaluate each model based on mean intersection over union (mIoU) and pixel-wise accuracy (PixAcc).

INR-Net-3 outperforms the equivalent FCN, and avoids confusing features such as shadows and road markings (Fig. 3). However, the performance deteriorates when we make the model deeper with a downsampling and upsampling layer (INR-Net-5), and the FCN surpasses both INR-Nets (Table 2). This echoes the difficulty in scaling INR-Nets observed in classification, and suggests that additional innovations in architecture or training methods may be needed to develop deeper INR-Nets.

6 Analysis

Using INR-Net with high-discrepancy sequences In many applications, there are large regions of the domain Ω that are less informative for the task of interest. For example, most of the information in 3D scenes is concentrated at object surfaces, so INR-Nets should not need to process a NeRF by densely sampling all 5 dimensions. Moreover, ground truth labels for dense prediction tasks may only be available along a high discrepancy point set. We find that even when we replace QMC with sample means over high discrepancy sequences, INR-Net’s performance on classification is not compromised. What seems to matter is that the model uses point sequences of similar discrepancy at training and test time. Details of our analysis are in Appendix E.1.

Initialization with discrete networks When an INR-Net is initialized with a large pre-trained discrete network, its outputs are similar⁵ by construction. However, the behavior of the pre-trained network is not preserved when the INR-Net switches to QMC – even tiny perturbations from the regular grid are sufficient to change a classifier’s predictions. Although the effect on the output of a single layer is much lower than the signal, small differences in each layer accumulate to exert a

⁵The accumulation of floating-point errors results in a small but noticeable difference in the final result, even with double precision.

large influence on the final output. In addition, we find that once grid sampling is abandoned, large INR-Nets cannot easily be fine-tuned to restore the behavior of the discrete network used to initialize it. This suggests that the optimization landscape of INR-Nets may differ substantially from that of discrete networks, and perhaps the approach for learning maps between L^2 functions requires fundamentally different strategies than those for learning maps between discrete functions, even when the functions represent the same underlying signals. Details of our analysis are in Appendix E.2.

7 Discussion and Limitations

Although designed for implicit neural data, INR-Net need not be trained on INRs. Our framework is sound for any data that can be represented as piecewise smooth integrable functions over a wide class of domains. Thus our approach may find use in deep learning systems that process a signal by querying it on a selected subset of its domain.

Error propagation When an INR does not faithfully represent the underlying data, it is important to characterize the influence on INR-Net’s output. In the worst case, these deviations are adversarial examples, and robustness techniques for discrete networks can also be applied to INR-Net. But what can we say about typical deviations of INRs? Future work should analyze patterns in the mistakes that different types of INRs make, and how to make INR-Nets robust to these.

Inseparable outputs An INR output of an INR-Net cannot be detached from the network without sacrificing the ability to evaluate it anywhere on its domain. INR-Net should be used cautiously in privacy-sensitive applications, as the model’s outputs may expose the network and upstream data. Future work should complement our framework with a method for efficiently translating output INRs to a new parameterization, such as co-training INR-Net with a hypernetwork.

8 Conclusion

INR-Nets constitute the first unified approach for performing inference directly on implicit neural representations. INR-Nets are parameterization-agnostic, universal approximators of a wide class of functions, and use numerical integration to achieve fast robust predictions. With the increasing popularity and diversity of INRs, as well as the emergence of tools to efficiently create large datasets of INRs, the time is ripe for a universal framework for learning on neural implicit datasets.

Acknowledgements

We thank Daniel Moyer and Nalini Singh for their proofreading and extensive comments. We thank Wei-Chiu Ma for pointing out the work in [16] and offering tips on continuous convolutions. Clinton gratefully acknowledges his funding from the Takeda Fellowship. This work was also supported in part by NIH NICHD under Grant R01HD100009, NIH NINDS under Grant U19NS115388, NIH NIBIB NAC under Grant P41EB015902.

References

- [1] Christoph Aistleitner and Josef Dick. Low-discrepancy point sets for non-uniform measures, 2013. URL <https://arxiv.org/abs/1308.5049>.
- [2] Alex Yu and Sara Fridovich-Keil, Matthew Tancik, Qinhong Chen, Benjamin Recht, and Angjoo Kanazawa. Plenoxels: Radiance fields without neural networks, 2021.
- [3] Alexandre Boulch. Generalizing discrete convolutions for unstructured point clouds. *CoRR*, abs/1904.02375, 2019. URL <http://arxiv.org/abs/1904.02375>.
- [4] Luca Brandolini, Leonardo Colzani, Giacomo Gigante, and Giancarlo Travaglini. On the koksma–hlawka inequality. *Journal of Complexity*, 29(2):158–172, 2013. ISSN 0885-064X. doi: <https://doi.org/10.1016/j.jco.2012.10.003>. URL <https://www.sciencedirect.com/science/article/pii/S0885064X12000854>.
- [5] Russel E Cafilisch. Monte carlo and quasi-monte carlo methods. *Acta numerica*, 7:1–49, 1998.
- [6] Tianping Chen and Hong Chen. Approximations of continuous functionals by neural networks with application to dynamic systems. *IEEE Transactions on Neural networks*, 4(6):910–918, 1993.
- [7] Tianping Chen, Hong Chen, and Ruey wen Liu. Approximation capability in $c(r/\sup n)$ by multilayer feedforward networks and related problems. *IEEE Transactions on Neural Networks*, 6(1):25–30, 1995. doi: 10.1109/72.363453.
- [8] Marius Cordts, Mohamed Omran, Sebastian Ramos, Timo Rehfeld, Markus Enzweiler, Rodrigo Benenson, Uwe Franke, Stefan Roth, and Bernt Schiele. The cityscapes dataset for semantic urban scene understanding. In *Proc. of the IEEE Conference on Computer Vision and Pattern Recognition (CVPR)*, 2016.
- [9] Abril Corona-Figueroa, Jonathan Frawley, Sam Bond-Taylor, Sarath Bethapudi, Hubert P. H. Shum, and Chris G. Willcocks. Mednerf: Medical neural radiance fields for reconstructing 3d-aware ct-projections from a single x-ray, 2022. URL <https://arxiv.org/abs/2202.01020>.
- [10] J. Deng, W. Dong, R. Socher, L.-J. Li, K. Li, and L. Fei-Fei. ImageNet: A Large-Scale Hierarchical Image Database. In *CVPR09*, 2009.
- [11] Emilien Dupont, Yee Whye Teh, and Arnaud Doucet. Generative models as distributions of functions. *CoRR*, abs/2102.04776, 2021. URL <https://arxiv.org/abs/2102.04776>.
- [12] Emilien Dupont, Hyunjik Kim, SM Eslami, Danilo Rezende, and Dan Rosenbaum. From data to functa: Your data point is a function and you should treat it like one. *arXiv preprint arXiv:2201.12204*, 2022.
- [13] Johann Engelbrecht*, Igor Fedotov, Tanya Fedotova, and Ansie Harding. Error bounds for quadrature methods involving lower order derivatives. *International Journal of Mathematical Education in Science and Technology*, 34(6):831–846, 2003. doi: 10.1080/00207390310001595429. URL <https://doi.org/10.1080/00207390310001595429>.
- [14] Logan Engstrom, Andrew Ilyas, Hadi Salman, Shibani Santurkar, and Dimitris Tsipras. Robustness (python library), 2019. URL <https://github.com/MadryLab/robustness>.
- [15] Matthias Fey, Jan Eric Lenssen, Frank Weichert, and Heinrich Müller. Splinecnn: Fast geometric deep learning with continuous b-spline kernels. *CoRR*, abs/1711.08920, 2017. URL <http://arxiv.org/abs/1711.08920>.
- [16] Ruohan Gao, Yen-Yu Chang, Shivani Mall, Li Fei-Fei, and Jiajun Wu. Objectfolder: A dataset of objects with implicit visual, auditory, and tactile representations. In *CoRL*, 2021.
- [17] Ruohan Gao, Zilin Si, Yen-Yu Chang, Samuel Clarke, Jeannette Bohg, Li Fei-Fei, Wenzhen Yuan, and Jiajun Wu. Objectfolder 2.0: A multisensory object dataset for sim2real transfer, 2022. URL <https://arxiv.org/abs/2204.02389>.
- [18] Kurt Hornik. Approximation capabilities of multilayer feedforward networks. *Neural networks*, 4(2):251–257, 1991.
- [19] Abhijit Kundu, Kyle Genova, Xiaoqi Yin, Alireza Fathi, Caroline Pantofaru, Leonidas Guibas, Andrea Tagliasacchi, Frank Dellaert, and Thomas Funkhouser. Panoptic neural fields: A semantic object-aware neural scene representation, 2022. URL <https://arxiv.org/abs/2205.04334>.

- [20] Moshe Leshno, Vladimir Ya Lin, Allan Pinkus, and Shimon Schocken. Multilayer feedforward networks with a nonpolynomial activation function can approximate any function. *Neural networks*, 6(6):861–867, 1993.
- [21] Zhuang Liu, Hanzi Mao, Chao-Yuan Wu, Christoph Feichtenhofer, Trevor Darrell, and Saining Xie. A convnet for the 2020s. *CoRR*, abs/2201.03545, 2022. URL <https://arxiv.org/abs/2201.03545>.
- [22] Ilya Loshchilov and Frank Hutter. Fixing weight decay regularization in adam. *CoRR*, abs/1711.05101, 2017. URL <http://arxiv.org/abs/1711.05101>.
- [23] Zhou Lu, Hongming Pu, Feicheng Wang, Zhiqiang Hu, and Liwei Wang. The expressive power of neural networks: A view from the width. *Advances in neural information processing systems*, 30, 2017.
- [24] Julien NP Martel, David B Lindell, Connor Z Lin, Eric R Chan, Marco Monteiro, and Gordon Wetzstein. Acorn: Adaptive coordinate networks for neural scene representation. *arXiv preprint arXiv:2105.02788*, 2021.
- [25] Lars M. Mescheder, Michael Oechsle, Michael Niemeyer, Sebastian Nowozin, and Andreas Geiger. Occupancy networks: Learning 3d reconstruction in function space. *CoRR*, abs/1812.03828, 2018. URL <http://arxiv.org/abs/1812.03828>.
- [26] Ben Mildenhall, Pratul P. Srinivasan, Matthew Tancik, Jonathan T. Barron, Ravi Ramamoorthi, and Ren Ng. Nerf: Representing scenes as neural radiance fields for view synthesis. *CoRR*, abs/2003.08934, 2020. URL <https://arxiv.org/abs/2003.08934>.
- [27] Thomas Müller, Alex Evans, Christoph Schied, and Alexander Keller. Instant neural graphics primitives with a multiresolution hash encoding. *arXiv:2201.05989*, January 2022.
- [28] Norman Müller, Andrea Simonelli, Lorenzo Porzi, Samuel Rota Bulò, Matthias Nießner, and Peter Kotschieder. Autorf: Learning 3d object radiance fields from single view observations, 2022. URL <https://arxiv.org/abs/2204.03593>.
- [29] Michael Niemeyer and Andreas Geiger. Giraffe: Representing scenes as compositional generative neural feature fields. In *Proc. IEEE Conf. on Computer Vision and Pattern Recognition (CVPR)*, 2021.
- [30] Michael Niemeyer, Lars Mescheder, Michael Oechsle, and Andreas Geiger. Occupancy flow: 4d reconstruction by learning particle dynamics. In *Proceedings of the IEEE/CVF international conference on computer vision*, pages 5379–5389, 2019.
- [31] Michael Niemeyer, Lars Mescheder, Michael Oechsle, and Andreas Geiger. Differentiable volumetric rendering: Learning implicit 3d representations without 3d supervision. In *Proc. IEEE Conf. on Computer Vision and Pattern Recognition (CVPR)*, 2020.
- [32] Jeong Joon Park, Peter Florence, Julian Straub, Richard A. Newcombe, and Steven Lovegrove. Deepsdf: Learning continuous signed distance functions for shape representation. *CoRR*, abs/1901.05103, 2019. URL <http://arxiv.org/abs/1901.05103>.
- [33] David W. Romero, Robert-Jan Brintjies, Jakub M. Tomczak, Erik J. Bekkers, Mark Hoogendoorn, and Jan C. van Gemert. Flexconv: Continuous kernel convolutions with differentiable kernel sizes. *CoRR*, abs/2110.08059, 2021. URL <https://arxiv.org/abs/2110.08059>.
- [34] David W. Romero, Anna Kuzina, Erik J. Bekkers, Jakub M. Tomczak, and Mark Hoogendoorn. Ckconv: Continuous kernel convolution for sequential data. *CoRR*, abs/2102.02611, 2021. URL <https://arxiv.org/abs/2102.02611>.
- [35] Vincent Sitzmann, Michael Zollhöfer, and Gordon Wetzstein. Scene representation networks: Continuous 3d-structure-aware neural scene representations. *CoRR*, abs/1906.01618, 2019. URL <http://arxiv.org/abs/1906.01618>.
- [36] Vincent Sitzmann, Eric R. Chan, Richard Tucker, Noah Snively, and Gordon Wetzstein. Metasdf: Meta-learning signed distance functions. *CoRR*, abs/2006.09662, 2020. URL <https://arxiv.org/abs/2006.09662>.
- [37] Vincent Sitzmann, Julien N. P. Martel, Alexander W. Bergman, David B. Lindell, and Gordon Wetzstein. Implicit neural representations with periodic activation functions. *CoRR*, abs/2006.09661, 2020. URL <https://arxiv.org/abs/2006.09661>.

- [38] Vincent Sitzmann, Semon Rezchikov, William T. Freeman, Joshua B. Tenenbaum, and Frédo Durand. Light field networks: Neural scene representations with single-evaluation rendering. *CoRR*, abs/2106.02634, 2021. URL <https://arxiv.org/abs/2106.02634>.
- [39] Mingxing Tan and Quoc V. Le. Efficientnet: Rethinking model scaling for convolutional neural networks. *CoRR*, abs/1905.11946, 2019. URL <http://arxiv.org/abs/1905.11946>.
- [40] Matthew Tancik, Ben Mildenhall, Terrance Wang, Divi Schmidt, Pratul P. Srinivasan, Jonathan T. Barron, and Ren Ng. Learned initializations for optimizing coordinate-based neural representations. *CoRR*, abs/2012.02189, 2020. URL <https://arxiv.org/abs/2012.02189>.
- [41] Matthew Tancik, Pratul P. Srinivasan, Ben Mildenhall, Sara Fridovich-Keil, Nithin Raghavan, Utkarsh Singhal, Ravi Ramamoorthi, Jonathan T. Barron, and Ren Ng. Fourier features let networks learn high frequency functions in low dimensional domains. *CoRR*, abs/2006.10739, 2020. URL <https://arxiv.org/abs/2006.10739>.
- [42] Benjamin Ummerhofer, Lukas Prantl, Nils Thuerey, and Vladlen Koltun. Lagrangian fluid simulation with continuous convolutions. In *International Conference on Learning Representations*, 2019.
- [43] Shenlong Wang, Simon Suo, Wei-Chiu Ma, Andrei Pokrovsky, and Raquel Urtasun. Deep parametric continuous convolutional neural networks. *CoRR*, abs/2101.06742, 2021. URL <https://arxiv.org/abs/2101.06742>.

Appendix

Appendix A provides additional background on quasi-Monte Carlo integration and low discrepancy sequences, including details about the conditions under which our theoretical results hold. Appendix B provides proofs of the Universal Approximator and Convergent Empirical Gradients properties, as well as extensions of these properties from the single-channel case stated in the main text to multi-channel maps. Appendix C provides a detailed specification of INR-Net layers that enable INR-Nets to replicate the behavior of many discrete networks. Appendix D describes the implicit neural datasets used in our experiments and the architectures of our INR-Nets. Appendix E provides additional details on our analysis in Section 6, demonstrating properties of INR-Nets under different sampling schemes.

A Quasi-Monte Carlo integration and low discrepancy sequences

Definition 1 (Koksma–Hlawka inequality) A function $f \in L^2(\Omega)$ satisfies a Koksma–Hlawka inequality if for any point set $\{x_j : x_j \in \Omega\}$,

$$\left| \frac{1}{N} \sum_{j=1}^N f(x_j) - \int_{\Omega} f(x) dx \right| \leq V(f) D(X), \quad (8)$$

for normalized measure dx , some notion of variation V of the function and some notion of discrepancy D of the point set.

The classical inequality gives a tight error bound for functions of bounded variation in the sense of Hardy-Krause (BVHK), a generalization of bounded variation to multivariate functions on $[0, 1]^d$ which has bounded variation in each variable. Specifically, the variation is defined as:

$$V_{HK}(f) = \sum_{\alpha \in \{0,1\}^d} \int_{[0,1]^{|\alpha|}} \left| \frac{\partial^\alpha}{\partial x^\alpha} f(x_\alpha) \right| dx, \quad (9)$$

with $\{0, 1\}^d$ the multi-indices and $x_\alpha \in [0, 1]^d$ such that $x_{\alpha,j} = x_j$ if $j \in \alpha$ and $x_{\alpha,j} = 1$ otherwise. The classical inequality also uses the star discrepancy of the point set X , given by:

$$D^*(X) = \sup_{I \in J} \left| \frac{1}{N} \sum_{j=1}^N \mathbb{1}(x_j \in I) - \mu(I) \right|, \quad (10)$$

where J is the set of d -dimensional intervals that include the origin, and μ the Lebesgue measure.

A point set is called low discrepancy if its discrepancy is on the order of $O((\ln N)^d/N)$. Quasi-Monte Carlo calculates the sample mean using a low discrepancy sequence (see Fig. A.1 for examples in 2D), as opposed to the i.i.d. point set generated by standard Monte Carlo, which will generally be high discrepancy. Because the Koksma–Hlawka inequality is sharp, when estimating the integral of a BVHK function on $[0, 1]^d$, the error of the QMC approximation decays as $O((\ln N)^d/N)$, in contrast to the error of the standard Monte Carlo approximation that decays as $O(N^{-1/2})$ [5].

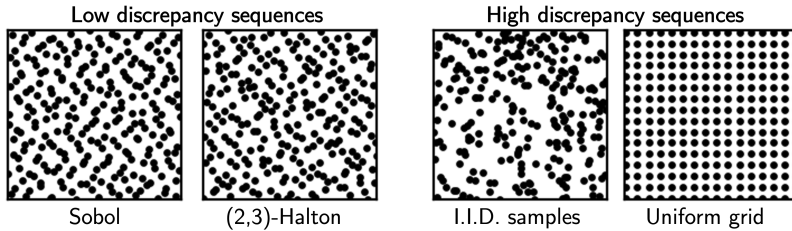


Figure A.1: Examples of low and high discrepancy sequences in 2D.

However, BVHK is a rather restrictive class of functions defined on $[0, 1]^d$ that excludes all functions with discontinuities. Brandolini et al. [4] extended the Koksma–Hlawka inequality to two classes of functions defined below:

Piecewise smooth functions Let f be a smooth function on $[0, 1]^d$ and Ω a Borel subset of $[0, 1]^d$. Then $f|_{\chi_\Omega}$ is a piecewise smooth function with the Koksma–Hlawka inequality given by total variation

$$V(f) = \sum_{\alpha \in \{0,1\}^d} 2^{d-|\alpha|} \int_{[0,1]^d} \left| \frac{\partial^\alpha f(x)}{\partial x^\alpha} \right| dx, \quad (11)$$

and discrepancy

$$D(X) = 2^d \sup_{I \subseteq [0,1]^d} \left| \frac{1}{N} \sum_{j=1}^N \mathbb{1}(x_j \in \Omega \cap I) - \mu(\Omega \cap I) \right|. \quad (12)$$

$W^{d,1}$ functions on manifolds Let \mathcal{M} be a smooth compact d -dimensional manifold with normalized measure dx . Given local charts $\{\phi_k\}_{k=1}^K$, $\phi_k : [0, 1]^d \rightarrow \mathcal{M}$, the variation of a function $f \in W^{d,1}(\mathcal{M})$ is characterized as:

$$V(f) = c \sum_{k=1}^K \sum_{|\alpha| \leq n} \int_{[0,1]^d} \left| \frac{\partial^\alpha}{\partial x^\alpha} (\psi_k(\phi_k(x)) f(\phi_k(x))) \right| dx, \quad (13)$$

with $\{\psi_k\}_{k=1}^K$ a smooth partition of unity subordinate to the charts, and constant $c > 0$ that depends on the charts, but not on f or μ . Defining the set of intervals in \mathcal{M} as $J = \{U : U = \phi_k(I) \text{ for some } k, I \subseteq [0, 1]^d\}$, with measure $\mu(U) = dx(I)$, the discrepancy of a point set $Y = \{y_j\}_{j=1}^N$ on \mathcal{M} is:

$$D(Y) = \sup_{U \in J} \left| \frac{1}{N} \sum_{j=1}^N \mathbb{1}(y_j \in U) - \mu(U) \right|. \quad (14)$$

The notion of discrepancy is not limited to the Lebesgue measure. The existence of low discrepancy point sets has been proven for non-negative, normalized Borel measure on $[0, 1]^d$ due to Aistleitner and Dick [1]. An extension of our framework to non-uniform measures is a promising direction for future work (see Section 6).

B Proofs

B.1 Proof of Property 2 (Universal Approximator)

Definition 2 Let $\mathcal{G}, \mathcal{G}'$ be subsets of $L^2(\Omega)$ restricted to compactly supported functions of absolute bounded variation. By this we mean there exists V^* such that every $f \in \mathcal{G} \cup \mathcal{G}'$ satisfies a Koksma–Hlawka inequality (8) with $V(|f|) < V^*$.

$\mathcal{G}, \mathcal{G}'$ are bounded in L^1 norm since all their functions are compactly supported and bounded.

Consider a Lipschitz continuous map $\mathcal{R} : \mathcal{G} \rightarrow \mathcal{G}'$ such that $d(\mathcal{R}[f], \mathcal{R}[g])_{L^1} \leq M_0 d(f, g)_{L^1}$ for some constant M_0 and all $f, g \in \mathcal{G}$. Let $M = \max\{M_0, 1\}$.

Select a fixed point set $X = \{x_j\}_{j=1}^N$ in Ω with discrepancy $D(X) = \frac{\epsilon}{12(M+2)V^*}$. By (8) this yields:

$$\left| \frac{1}{N} \sum_{j=1}^N f(x_j) - \int_{\Omega} f(x) dx \right| \leq \frac{\epsilon}{12(M+2)}, \quad (15)$$

for all $f \in \mathcal{G} \cup \mathcal{G}'$.

Definition 3 The projection $\pi : f \mapsto \mathbf{f}$ is a quotient map $L^2(\Omega) \rightarrow L^2(\Omega)/\sim$ under the equivalence relation $f \sim g$ iff $f(x_j) = g(x_j)$ for all $x_j \in X$.

$L^2(\Omega)/\sim$ can be identified with \mathbb{R}^N , and thus can be given the normalized ℓ^1 norm:

$$\|\pi f\|_{\ell^1} = \frac{1}{N} \sum_{j=1}^N |f(x_j)|. \quad (16)$$

Definition 4 Denote the preimage of π as $\pi^{-1} : \mathbf{f}' \mapsto \{f' \in \mathcal{G}' : \pi f' = \mathbf{f}'\}$. Invoking the axiom of choice, define the inverse projection $\pi^{-1} : \pi \mathcal{G}' \rightarrow \mathcal{G}'$ by a choice function over the sets $\pi^{-1}(\pi \mathcal{G}')$.

Remark: Note that this inverse projection corresponds to some way of interpolating the N sample points such that the output is in \mathcal{G}' . Although our definition implies the existence of such an interpolator, we leave its specification as an open problem. Since Ω only permits discontinuities along a fixed Borel subset of $[0, 1]^d$, these boundaries can be specified *a priori* in the interpolator. Since all functions in \mathcal{G}' are bounded and continuous outside this set, the interpolator can be represented by a bounded continuous map, hence it is expressible by an INR-Net layer.

Definition 5 π generates a σ -algebra on \mathcal{G} given by $\mathcal{A} = \{\pi^{-1}(S) : S \in \mathcal{L}\}$, with \mathcal{L} the σ -algebra of Lebesgue measurable sets on \mathbb{R}^N . Because this σ -algebra depends on ϵ and the Lipschitz constant of \mathcal{R} via the point set discrepancy, we may write it as $\mathcal{A}_{\epsilon, \mathcal{R}}$.

Remark: In this formulation, we let the tolerance ϵ and the Lipschitz constant of \mathcal{R} dictate what subsets of \mathcal{G} are measurable, and thus which measures on \mathcal{G} are permitted. However, if the desired measure ν is more fine-grained than what is permitted by $\mathcal{A}_{\epsilon, \mathcal{R}}$, then it is ν that should determine the number of QMC samples N , rather than ϵ or \mathcal{R} .

We now state the following lemmas which will be used to prove our universal approximation theorem.

Lemma 1 There is a map $\tilde{\mathcal{R}} : \pi\mathcal{G} \rightarrow \pi\mathcal{G}'$ such that

$$\int_{\Omega} \left| \mathcal{R}[f](x) - \pi^{-1} \circ \tilde{\mathcal{R}} \circ \pi[f](x) \right| dx = \frac{\epsilon}{6}. \quad (17)$$

Proof: Let $g(x) = |f(x)|$ for $f \in \mathcal{G} \cup \mathcal{G}'$. Because (15) applies to $g(x)$, we have:

$$\left| \frac{1}{N} \sum_{j=1}^N g(x_j) - \int_{\Omega} g(x) dx \right| \leq \frac{\epsilon}{12(M+2)} \quad (18)$$

$$\left| \|\pi f\|_{\ell^1} - \|f\|_{L^1} \right| \leq \frac{\epsilon}{12(M+2)}. \quad (19)$$

Eqn. (19) also implies that for any $\mathbf{f} \in \pi\mathcal{G} \cup \pi\mathcal{G}'$, we have:

$$\left| \|\mathbf{f}\|_{\ell^1} - \|\pi^{-1}\mathbf{f}\|_{L^1} \right| \leq \frac{\epsilon}{12(M+2)}. \quad (20)$$

Combining (19) and (20), we obtain

$$\left| \|f\|_{L^1} - \|\pi^{-1} \circ \pi[f]\|_{L^1} \right| \leq \frac{\epsilon}{6(M+2)}. \quad (21)$$

By the triangle inequality and applying \mathcal{R} :

$$\int_{\Omega} \left| \mathcal{R}[f](x) - \pi^{-1} \circ \pi \circ \mathcal{R}[f](x) \right| dx \leq \frac{\epsilon}{6(M+2)}. \quad (22)$$

For any $f, g \in \mathcal{G}$ such that $\pi f = \pi g$, (19) tells us that $d(f, g)_{L^1}$ is at most $\epsilon/6(M+2)$. Recall M was defined such that $d(\mathcal{R}[f], \mathcal{R}[g])_{L^1} \leq M d(f, g)_{L^1}$ for any \mathcal{R} .

$$d(\pi \circ \mathcal{R}[f], \pi \circ \mathcal{R}[g])_{L^1} \leq \frac{M\epsilon}{6(M+2)} + \frac{\epsilon}{6(M+2)} \quad (23)$$

$$= \frac{(M+1)\epsilon}{(M+2)6} \quad (24)$$

So defining:

$$\tilde{\mathcal{R}} = \arg \min_{\mathcal{H}} d(\mathcal{H} \circ \pi[f], \pi \circ \mathcal{R}[f])_{\ell^1}, \quad (25)$$

we have

$$\left| \tilde{\mathcal{R}} \circ \pi[f] - \pi \circ \mathcal{R}[f] \right| \leq \frac{(M+1)\epsilon}{(M+2)6}. \quad (26)$$

Then by (22),

$$\int_{\Omega} \left| \mathcal{R}[f](x) - \pi^{-1} \circ \tilde{\mathcal{R}} \circ \pi[f](x) \right| dx \leq \frac{\epsilon}{6(M+2)} + \frac{(M+1)\epsilon}{(M+2)6} \quad (27)$$

$$= \frac{\epsilon}{6}. \quad (28)$$

□

Lemma 2 Consider the extension of $\tilde{\mathcal{R}}$ to $\mathbb{R}^N \rightarrow \mathbb{R}^N$ in which each component of the output has the form:

$$\tilde{\mathcal{R}}_j(\mathbf{f}) = \begin{cases} \mathcal{R}[\pi^{-1}\mathbf{f}](x_j) & \text{if } \mathbf{f} \in \pi\mathcal{G} \\ 0 & \text{otherwise.} \end{cases} \quad (29)$$

Then any finite measure ν on the measurable space $(\mathcal{G}, \mathcal{A})$ induces a finite measure μ on $(\mathbb{R}^N, \mathcal{L})$, and $\int_{\mathbb{R}^N} |\tilde{\mathcal{R}}_j(\mathbf{f})| \mu(d\mathbf{f}) < \infty$ for each j .

Proof: Since the σ -algebra \mathcal{A} on \mathcal{G} is generated by π , the measure $\mu : \mu(\pi S) = \nu(S)$ for all $S \in \mathcal{A}$ is finite and defined w.r.t. the Lebesgue measurable sets on $\pi\mathcal{G}$. Since $\pi\mathcal{G}$ can be identified with a measurable subset of \mathbb{R}^N , μ can be naturally extended to \mathbb{R}^N . Doing so makes it absolutely continuous w.r.t. the Lebesgue measure on \mathbb{R}^N .

To show $\tilde{\mathcal{R}}_j(\mathbf{f})$ is integrable, it is sufficient to show it is bounded and compactly supported.

\mathcal{G} is bounded in the L^1 norm. Thus by (19), $\pi\mathcal{G}$ is bounded in the normalized ℓ_1 norm. The ℓ_1 norm in \mathbb{R}^N is strongly equivalent to the uniform norm, so there is some compact set $[-c, c]^N$, $c > 0$ for which the extension of $\pi\mathcal{G}$ to \mathbb{R}^N vanishes, so $\text{supp}(\tilde{\mathcal{R}}_j(\mathbf{f})) \subseteq [-c, c]^N$.

Similarly, $\pi\mathcal{G}'$ is bounded in the ℓ^1 norm, hence there exists c' such that $\tilde{\mathcal{R}}_j < c'$ for all j . □

Lemma 3 For any finite measure μ absolutely continuous w.r.t. the Lebesgue measure on \mathbb{R}^n , $J \in L^1(\mu)$ and $\epsilon > 0$, there is a network \mathcal{K} such that:

$$\int_{\mathbb{R}^n} |J(\mathbf{f}) - \mathcal{K}(\mathbf{f})| \mu(d\mathbf{f}) < \frac{\epsilon}{2}. \quad (30)$$

Proof: The following construction is adapted from Lu et al. [23]. Since J is integrable, there is a cube $E = [-c, c]^n$ such that:

$$\int_{\mathbb{R}^n \setminus E} |J(\mathbf{f})| \mu(d\mathbf{f}) < \frac{\epsilon}{8} \quad (31)$$

$$\|J - \mathbb{1}_E J\|_1 < \frac{\epsilon}{8}. \quad (32)$$

Case 1: J is non-negative on all of \mathbb{R}^n

Define the set under the graph of $J|_E$:

$$G_{E,J} \triangleq \{(\mathbf{f}, y) : \mathbf{f} \in E, y \in [0, J(\mathbf{f})]\}. \quad (33)$$

$G_{E,J}$ is compact in \mathbb{R}^{n+1} , hence there is a finite cover of open rectangles $\{R'_i\}$ satisfying $\mu(\cup_i R'_i) - \mu(G_{E,J}) < \frac{\epsilon}{8}$ on \mathbb{R}^n . Take their closures, and extend the sides of all rectangles indefinitely. This results in a set of pairwise almost disjoint rectangles $\{R_i\}$. Taking only the rectangles $R = \{R_i : \mu(R_i \cap G_{E,J}) > 0\}$ results in a finite cover satisfying:

$$\sum_{i=1}^{|R|} \mu(R_i) - \mu(G_{E,J}) < \frac{\epsilon}{8}. \quad (34)$$

This implies:

$$\sum_{i=1}^{|R|} \mu(R_i) < \|J\|_1 + \frac{\epsilon}{8}, \quad (35)$$

and also,

$$\frac{\epsilon}{8} > \sum_{i=1}^{|R|} \int_{\mathbb{R}^n} \mathbb{1}_{R_i}(\mathbf{f}, J(\mathbf{f})) \mu(d\mathbf{f}) + \|J\|_1 \quad (36)$$

$$\geq \int_E |J(\mathbf{f}) - \sum_{i=1}^{|R|} \mathbb{1}_{R_i}(\mathbf{f}, J(\mathbf{f}))| \mu(d\mathbf{f}), \quad (37)$$

by the triangle inequality. For each $R_i = [a_{i1}, b_{i1}] \times \dots \times [a_{in}, b_{in}] \times [\zeta_i, \zeta_i + y_i]$, let X_i be its first n components (i.e., the projection of R_i onto \mathbb{R}^n). Then we have

$$\int_E |J(\mathbf{f}) - \sum_{i=1}^{|R|} y_i \mathbb{1}_{X_i}(\mathbf{f})| \mu(d\mathbf{f}) < \frac{\epsilon}{8}. \quad (38)$$

Let $Y(\mathbf{f}) \triangleq \sum_{i=1}^{|R|} y_i \mathbb{1}_{X_i}(\mathbf{f})$. By the triangle inequality,

$$\int_{\mathbb{R}^n} |J(\mathbf{f}) - \mathcal{K}(\mathbf{f})| \mu(d\mathbf{f}) \leq \|J - \mathbb{1}_E J\|_1 + \|\mathbb{1}_E J - Y\|_1 + \|\mathcal{K} - Y\|_1 \quad (39)$$

$$< \frac{\epsilon}{4} + \|\mathcal{K} - Y\|_1, \quad (40)$$

by (32) and (38). So it remains to construct \mathcal{K} such that $\|\mathcal{K} - Y\|_1 < \frac{\epsilon}{4}$. Because $\mathbb{1}_{X_i}$ is discontinuous at the boundary of the rectangle X_i , it cannot be produced directly from an INR-Net (recall that all layers are continuous maps). However, we can approximate it arbitrarily well with a piece-wise linear function that rapidly ramps from 0 to 1 at the boundary.

For fixed rectangle X_i and $\delta \in (0, 0.5)$, consider the inner rectangle $X_\delta \subset X_i$:

$$X_\delta = (a_1 + \delta(b_1 - a_1), b_1 - \delta(b_1 - a_1)) \times \dots \times (a_n + \delta(b_n - a_n), b_n - \delta(b_n - a_n)), \quad (41)$$

where we omit subscript j for clarity. Letting $b'_i = b_i - \delta(b_i - a_i)$, define the function:

$$T(\mathbf{f}) = \prod_{i=1}^n \frac{1}{\delta} [\text{ReLU}(\delta - \text{ReLU}(\mathbf{f}_i - b'_i)) - \text{ReLU}(\delta - \text{ReLU}(\mathbf{f}_i - a_i))], \quad (42)$$

where $\text{ReLU}(x) = \max(x, 0)$. $T(\mathbf{f})$ is a piece-wise linear function that ramps from 0 at the boundary of X_i to 1 within X_δ , and vanishes outside X_i . Note that

$$\|\mathbb{1}_X - T\|_1 < \mu(X) - \mu(X_\delta) \quad (43)$$

$$= (1 - (1 - 2\delta)^n) \mu(X), \quad (44)$$

if μ is the Lebesgue measure. δ may need to be smaller under other measures, but this adjustment is independent of the input \mathbf{f} so it can be specified *a priori*.

Recall that the function we want to approximate is $Y(\mathbf{f}) = \sum_{i=1}^{|R|} y_i \mathbb{1}_{X_i}(\mathbf{f})$. We can build INR-Net layers $\mathcal{K} : \mathbf{f} \mapsto \mathcal{K}(\mathbf{f}) = \sum_{i=1}^{|R|} y_i T_i(\mathbf{f})$, since this only involves linear combinations and ReLUs.

Then,

$$\|\mathcal{K} - Y\|_1 = \int_{\mathbb{R}^n} \sum_{i=1}^{|R|} y_i (T_i(\mathbf{f}) - \mathbb{1}_{X_i}(\mathbf{f})) d\mathbf{f} \quad (45)$$

$$= \sum_{i=1}^{|R|} y_i \|\mathbb{1}_{X_i} - T_i\|_1 \quad (46)$$

$$< (1 - (1 - 2\delta)^n) \sum_{i=1}^{|R|} y_i \mu(X_i) \quad (47)$$

$$= (1 - (1 - 2\delta)^n) \sum_{i=1}^{|R|} \mu(R_i) \quad (48)$$

$$< (1 - (1 - 2\delta)^n) \left(\|J\|_1 + \frac{\epsilon}{8} \right), \quad (49)$$

by (35). And so by choosing:

$$\delta = \frac{1}{2} \left(1 - \left(1 - \frac{\epsilon}{4} \left(\|J\|_1 + \frac{\epsilon}{8} \right)^{-1} \right)^{1/n} \right), \quad (50)$$

we have our desired bound $\|\mathcal{K} - Y\|_1 < \frac{\epsilon}{4}$ and thereby $\|J - \mathcal{K}\|_1 < \frac{\epsilon}{2}$.

Case 2: J is negative on some region of \mathbb{R}^n

Letting $J^+(\mathbf{f}) = \max(0, J(\mathbf{f}))$ and $J^-(\mathbf{f}) = \max(0, -J(\mathbf{f}))$, define:

$$G_{E,J}^+ \triangleq \{(\mathbf{f}, y) : \mathbf{f} \in E, y \in [0, J^+(\mathbf{f})]\} \quad (51)$$

$$G_{E,J}^- \triangleq \{(\mathbf{f}, y) : \mathbf{f} \in E, y \in [0, J^-(\mathbf{f})]\}. \quad (52)$$

As in (34), construct covers of rectangles R^+ over $G_{E,J}^+$ and R^- over $G_{E,J}^-$ each with bound $\frac{\epsilon}{16}$ and \mathbb{R}^n projections X^+, X^- . Let:

$$Y^+(\mathbf{f}) = \sum_{i=1}^{|R^+|} y_i^+ \mathbb{1}_{X_i^+}(\mathbf{f}) \quad (53)$$

$$Y^-(\mathbf{f}) = \sum_{i=1}^{|R^-|} y_i^- \mathbb{1}_{X_i^-}(\mathbf{f}) \quad (54)$$

$$Y = Y^+ - Y^- \quad (55)$$

We can derive an equivalent expression to (38):

$$\frac{\epsilon}{8} > \int_E |J(\mathbf{f}) - \sum_{i=1}^{|R^+|} y_i^+ \mathbb{1}_{X_i^+}(\mathbf{f}) + \sum_{i=1}^{|R^-|} y_i^- \mathbb{1}_{X_i^-}(\mathbf{f})| d\mathbf{f} \quad (56)$$

$$= \|\mathbb{1}_E J - Y\|_1. \quad (57)$$

Similarly to earlier, we use (32) and (57) to get:

$$\int_{\mathbb{R}^n} |J(\mathbf{f}) - \mathcal{K}(\mathbf{f})| d\mathbf{f} < \frac{\epsilon}{4} + \|\mathcal{K} - Y\|_1. \quad (58)$$

Choosing $T_i^+(\mathbf{f})$ and $T_i^-(\mathbf{f})$ the piece-wise linear functions associated with X_i^+ and X_i^- , and:

$$\mathcal{K}(\mathbf{f}) = \sum_{i=1}^{|R^+|} y_i^+ T_i^+(\mathbf{f}) - \sum_{i=1}^{|R^-|} y_i^- T_i^-(\mathbf{f}), \quad (59)$$

we have:

$$\|\mathcal{K} - Y\|_1 = \int_{\mathbb{R}^n} \left| \sum_{i=1}^{|R^+|} y_i^+ \left(T_i^+(\mathbf{f}) - \mathbb{1}_{X_i^+}(\mathbf{f}) \right) - \sum_{i=1}^{|R^-|} y_i^- \left(T_i^-(\mathbf{f}) - \mathbb{1}_{X_i^-}(\mathbf{f}) \right) \right| d\mathbf{f}, \quad (60)$$

applying the triangle inequality,

$$\leq \sum_{i=1}^{|R^+|} y_i^+ \left\| \mathbb{1}_{X_i^+} - T_i^+ \right\|_1 + \sum_{i=1}^{|R^-|} y_i^- \left\| \mathbb{1}_{X_i^-} - T_i^- \right\|_1 \quad (61)$$

$$< (1 - (1 - 2\delta^+)^n) \sum_{i=1}^{|R^+|} y_i^+ \mu(X_i^+) + (1 - (1 - 2\delta^-)^n) \sum_{i=1}^{|R^-|} y_i^- \mu(X_i^-) \quad (62)$$

$$< (1 - (1 - 2\delta^+)^n) \left(\|J^+\|_1 + \frac{\epsilon}{16} \right) + (1 - (1 - 2\delta^-)^n) \left(\|J^-\|_1 + \frac{\epsilon}{16} \right). \quad (63)$$

By choosing:

$$\delta^+ = \frac{1}{2} \left(1 - \left(1 - \frac{\epsilon}{8} \left(\|J^+\|_1 + \frac{\epsilon}{16} \right)^{-1} \right)^{1/n} \right) \quad (64)$$

$$\delta^- = \frac{1}{2} \left(1 - \left(1 - \frac{\epsilon}{8} \left(\|J^-\|_1 + \frac{\epsilon}{16} \right)^{-1} \right)^{1/n} \right), \quad (65)$$

and proceeding as before, we arrive at the same bounds $\|\mathcal{K} - Y\|_1 < \frac{\epsilon}{4}$ and $\|J - \mathcal{K}\|_1 < \frac{\epsilon}{2}$.

Putting it all together, Algorithm B.1 implements the network logic for producing the function \mathcal{K} .

Algorithm B.1 INR-Net approximation of $\mathbf{f} \mapsto J(\mathbf{f})$

Setup

Given target function J , L_1 tolerance $\epsilon/2$

Choose rectangles $R_i^+ = [a_{i1}^+, b_{i1}^+] \times \dots \times [a_{in}^+, b_{in}^+] \times [\zeta_i^+, \zeta_i^+ + y_i^+]$ satisfying (34) and R^- similarly

$$\delta^+ \leftarrow \frac{1}{16} \left(1 - (1 - \epsilon (\|J^+\|_1 + \frac{\epsilon}{16})^{-1})^{1/n} \right)$$

$$\delta^- \leftarrow \frac{1}{16} \left(1 - (1 - \epsilon (\|J^-\|_1 + \frac{\epsilon}{16})^{-1})^{1/n} \right)$$

Inference

Given discretized input $\mathbf{f} = \{\mathbf{f}_k\}_{k=1}^n$

$x \leftarrow (0, 0, 1, 0, 0)$

for rectangle $R_i^+ \in R^+$ **do**

for dimension $k \in 1 : n$ **do**

$x \leftarrow (\mathbf{f}_k - b_{ik}^+ + \delta(b_{ik}^+ - a_{ik}^+), \mathbf{f}_k - a_{ik}^+, x_3, x_4, x_5)$

$x \leftarrow \text{ReLU}(x)$

$x \leftarrow (\delta - x_1, \delta - x_2, x_3, x_4, x_5)$

$x \leftarrow \text{ReLU}(x)$

$x \leftarrow (0, 0, x_3(x_1 - x_2)/\delta, x_4, x_5)$

end

$x \leftarrow (0, 0, 1, y_i^+ x_3 + x_4, x_5)$

end

for rectangle $R_i^- \in R^-$ **do**

for dimension $k \in 1 : n$ **do**

$x \leftarrow (\mathbf{f}_k - b_{ik}^- + \delta(b_{ik}^- - a_{ik}^-), \mathbf{f}_k - a_{ik}^-, x_3, x_4, x_5)$

\dots

end

$x \leftarrow (0, 0, 1, x_4, y_i^- x_3 + x_5)$

end

return $x_4 - x_5$

We can provide x with access to \mathbf{f} either through skip connections or by appending channels with the values $\{c + \mathbf{f}_k\}_{k=1}^n$ (which will be preserved under ReLU). \square

Theorem 1 (Maps between Single-Channel INRs) *For any Lipschitz continuous map $\mathcal{R} : \mathcal{G} \rightarrow \mathcal{G}'$, any $\epsilon > 0$, and any finite measure ν w.r.t. the measurable space $(\mathcal{G}, \mathcal{A}_{\epsilon, \mathcal{R}})$, there exists an INR-Net \mathcal{T} that satisfies:*

$$\int_{\mathcal{G}} \|\mathcal{R}(f) - \mathcal{T}(f)\|_{L^1(\Omega)} \nu(df) < \epsilon. \quad (66)$$

Proof: If ν is not normalized, the discrepancy of our point set needs to be further divided by $\max\{\nu(\mathcal{G}), 1\}$. We assume for the remainder of this section that ν is normalized. Perform the construction of Lemma 3 N times, each with a tolerance of $\epsilon/2N$. Choose a partition of unity $\{\psi_j\}$ for which $\psi_j(x_k) = \delta_{jk}$, and output N channels with the values $\{\mathcal{K}_j(\mathbf{f})\psi_j(\cdot)\}_{j=1}^N$. By summing these channels we obtain a network $\tilde{\mathcal{K}}$ that fully specifies the desired behavior of $\tilde{\mathcal{R}} : \mathbb{R}^N \rightarrow \mathbb{R}^N$, with combined error:

$$\int_{\mathbb{R}^N} \|\tilde{\mathcal{R}}(\mathbf{f}) - \tilde{\mathcal{K}}(\mathbf{f})\|_{\ell^1} \mu(d\mathbf{f}) < \frac{\epsilon}{2}. \quad (67)$$

Thus,

$$\int_{\mathcal{G}} \left| \frac{1}{N} \sum_{j=1}^N \tilde{\mathcal{R}} \circ \pi[f](x_j) - \tilde{\mathcal{K}} \circ \pi[f](x_j) \right| \nu(df) \leq \frac{\epsilon}{2}. \quad (68)$$

By (20) we have:

$$\int_{\mathcal{G}} \left| \int_{\Omega} \left| \pi^{-1} \circ \tilde{\mathcal{R}} \circ \pi[f](x) - \pi^{-1} \circ \tilde{\mathcal{K}} \circ \pi[f](x) \right| dx \right| \nu(df) \leq \frac{\epsilon}{2} + \frac{\epsilon}{6(M+2)} \quad (69)$$

By Lemma 1 we have:

$$\int_{\mathcal{G}} \int_{\Omega} \left| \mathcal{R}[f](x) - \pi^{-1} \circ \tilde{\mathcal{K}} \circ \pi[f](x) \right| dx \nu(df) \leq \frac{\epsilon}{2} + \frac{\epsilon}{6(M+2)} + \frac{\epsilon}{6} \quad (70)$$

And thus the network $\mathcal{T} = \pi^{-1} \circ \tilde{\mathcal{K}} \circ \pi$ gives us the desired bound:

$$\int_{\mathcal{G}} \|\mathcal{R}(f) - \mathcal{T}(f)\|_{L^1(\Omega)} \nu(df) < \epsilon. \quad (71)$$

\square

Corollary 1 (Maps from INRs to vectors) *For any Lipschitz continuous map $\mathcal{R} : \mathcal{G} \rightarrow \mathbb{R}^n$, any $\epsilon > 0$, and any finite measure ν w.r.t. the measurable space $(\mathcal{G}, \mathcal{A}_{\epsilon, \mathcal{R}})$, there exists an INR-Net \mathcal{T} that satisfies:*

$$\int_{\mathcal{G}} \|\mathcal{R}(f) - \mathcal{T}(f)\|_{\ell^1(\mathbb{R}^n)} \nu(df) < \epsilon. \quad (72)$$

Proof: Let M_0 be the Lipschitz constant of \mathcal{R} in the sense that $d(\mathcal{R}[f], \mathcal{R}[g])_{\ell^1} \leq M_0 d(f, g)_{L^1}$. Let $M = \max\{M_0, 1\}$. There exists $\tilde{\mathcal{R}} : \pi\mathcal{G} \rightarrow \mathbb{R}^n$ such that $\|\tilde{\mathcal{R}} \circ \pi[f] - \mathcal{R}[f]\|_{\ell^1} \leq \epsilon/12$. As in Lemma 2, consider the extension of $\tilde{\mathcal{R}}$ to $\mathbb{R}^N \rightarrow \mathbb{R}^n$ in which each component of the output has the form:

$$\tilde{\mathcal{R}}_j(\mathbf{f}) = \begin{cases} \mathcal{R}[\pi^{-1}\mathbf{f}]_j & \text{if } \mathbf{f} \in \pi\mathcal{G} \\ 0 & \text{otherwise.} \end{cases} \quad (73)$$

Then for similar reasoning, ν on \mathcal{G} induces a measure μ on \mathbb{R}^N that is finite and absolutely continuous w.r.t. the Lebesgue measure, and $\int_{\mathbb{R}^N} |\tilde{\mathcal{R}}_j(\mathbf{f})| \mu(d\mathbf{f}) < \infty$ for each j .

We construct our $\mathbb{R}^N \rightarrow \mathbb{R}$ approximation n times with a tolerance of $\epsilon/2n$, such that:

$$\int_{\mathbb{R}^N} \left\| \tilde{\mathcal{R}}(\mathbf{f}) - \tilde{\mathcal{K}}(\mathbf{f}) \right\|_{\ell^1(\mathbb{R}^n)} \mu(d\mathbf{f}) < \frac{\epsilon}{2}. \quad (74)$$

Applying (19), we find that the network $\mathcal{T} = \tilde{\mathcal{K}} \circ \pi$ gives us the desired bound:

$$\int_{\mathcal{G}} \|\mathcal{R}(f) - \mathcal{T}(f)\|_{\ell^1(\mathbb{R}^n)} \nu(df) < \epsilon. \quad (75)$$

□

Corollary 2 (Maps from vectors to INRs) *For any Lipschitz continuous map $\mathcal{R} : \mathbb{R}^n \rightarrow \mathcal{G}$ and any $\epsilon > 0$, there exists an INR-Net \mathcal{T} that satisfies:*

$$\int_{\mathbb{R}^n} \|\mathcal{R}(x) - \mathcal{T}(x)\|_{L^1(\Omega)} dx < \epsilon. \quad (76)$$

Proof: Define the map $\tilde{\mathcal{R}} : \mathbb{R}^n \rightarrow \pi\mathcal{G} \subset \mathbb{R}^N$ by $\tilde{\mathcal{R}} = \pi \circ \mathcal{R}$. Since $\tilde{\mathcal{R}}$ is bounded and compactly supported, $\int_{\mathbb{R}^N} |\tilde{\mathcal{R}}_i(x)| dx < \infty$ for each i .

We construct a $\mathbb{R}^n \rightarrow \mathbb{R}$ approximation N times each with a tolerance of $\epsilon/2N$, such that:

$$\int_{\mathbb{R}^n} \left\| \tilde{\mathcal{R}}(x) - \tilde{\mathcal{K}}(x) \right\|_{L^1(\Omega)} dx < \frac{\epsilon}{2}. \quad (77)$$

Applying (20), we find that the network $\mathcal{T} = \pi^{-1} \circ \tilde{\mathcal{K}}$ gives us the desired bound:

$$\int_{\mathbb{R}^n} \|\mathcal{R}(x) - \mathcal{T}(x)\|_{L^1(\Omega)} dx < \epsilon. \quad (78)$$

□

Denote the space of multi-channel INRs as $\mathcal{F}_c = \{f : \Omega \rightarrow \mathbb{R}^c : \int_{\Omega} \|f\|_1 dx < \infty, f_i \in \mathcal{G} \text{ for each } i\}$. Denote the norm on this space as:

$$\|f\|_{\mathcal{F}_c} = \int_{\Omega} \sum_{i=1}^c |f_i(x)| dx. \quad (79)$$

\mathcal{F}_1 is identified with \mathcal{G} .

Definition 6 (Concatenation) *Concatenation is a map from two INR channels $f_i, f_j \in \mathcal{G}$ to $[f_i, f_j] \in \mathcal{F}_2$. The concatenation of INRs can be defined inductively to yield $\mathcal{F}_n \times \mathcal{F}_m \rightarrow \mathcal{F}_{n+m}$ for any $n, m \in \mathbb{N}$.*

Remark: All maps $\mathcal{F}_n \times \mathcal{F}_m \rightarrow \mathcal{F}_c$ can be expressed as a concatenation followed by a map $\mathcal{F}_{n+m} \rightarrow \mathcal{F}_c$. A map $\mathbb{R}^n \rightarrow \mathcal{F}_m$ is also equivalent to m maps $\mathbb{R}^n \rightarrow \mathcal{G}$ followed by concatenation. Thus, we need only characterize the maps that take one multi-channel INR as input.

Considering the maps $\mathcal{F}_n \rightarrow \mathcal{F}_m$, we choose a lower discrepancy point set X on Ω such that the Koksma–Hlawka inequality yields a bound of $\epsilon/12mn(M+2)$. Let π project each component of the input to $\pi\mathcal{G}$, and π^{-1} inverts this projection under some choice function. We take \mathcal{A}' to be the product σ -algebra generated from this π : $\mathcal{A}' = \{E_1 \times \cdots \times E_c : E_1, \dots, E_c \in \mathcal{A}\}$ where \mathcal{A} is the σ -algebra on \mathcal{G} from Definition 5.

Corollary 3 (Maps between multi-channel INRs) *For any Lipschitz continuous map $\mathcal{R} : \mathcal{F}_n \rightarrow \mathcal{F}_m$, any $\epsilon > 0$, and any finite measure ν w.r.t. the measurable space $(\mathcal{F}_n, \mathcal{A}'_{\epsilon, \mathcal{R}})$, there exists an INR-Net \mathcal{T} that satisfies:*

$$\int_{\mathcal{F}_n} \|\mathcal{R}(f) - \mathcal{T}(f)\|_{\mathcal{F}_m} \nu(df) < \epsilon. \quad (80)$$

Proof: The proof is very similar to that of Theorem 1. Our network now requires nN maps from $\mathbb{R}^{mN} \rightarrow \mathbb{R}$ each with error $\epsilon/2mnN$. Summing the errors across all input and output channels yields our desired bound. \square

The multi-channel analogue of Corollary 1 is clear, and we state it here for completeness:

Corollary 4 (Maps from multi-channel INRs to vectors) *For any Lipschitz continuous map $\mathcal{R} : \mathcal{F}_n \rightarrow \mathbb{R}^m$, any $\epsilon > 0$, and any finite measure ν w.r.t. the measurable space $(\mathcal{F}_n, \mathcal{A}'_{\epsilon, \mathcal{R}})$, there exists an INR-Net \mathcal{T} that satisfies:*

$$\int_{\mathcal{F}_n} \|\mathcal{R}(f) - \mathcal{T}(f)\|_{\ell_1(\mathbb{R}^m)} \nu(df) < \epsilon. \quad (81)$$

B.2 Proof of Property 3 (Convergent Empirical Gradients)

An INR-Net permits backpropagation of its outputs with respect to its input as well as all its learnable parameters. Within each layer, the gradients along a low discrepancy sequence in Ω , if they exist, converge to the appropriate derivative under the measure on Ω .

To establish convergence in the number of QMC samples N , let us suppose we have a family of sequences $\{X_N\}_{N \in \mathbb{N}} : X_N = \{x_j\}_{j=1}^N$ on Ω whose discrepancy converges to 0 as $N \rightarrow \infty$.

We note that no convergence statement is needed if the layer does not perform QMC integration. This includes layers which take \mathbb{R}^n as input, as well as point-wise transformations. Then the (sub)derivatives with respect to inputs and parameters need only be well-defined at each point of the output in order to enable backpropagation.

Thus we consider a layer \mathcal{H}_ϕ which takes an INR f as input. By (1) and (3), it can be written as:

$$\mathcal{H}_\phi[f] = \int_{\Omega} H_\phi[f](x) dx. \quad (82)$$

We write the QMC estimate of $\mathcal{H}_\phi[f]$ under X_N as:

$$\hat{H}_\phi^N[f] = \frac{1}{N} \sum_{j=1}^N H_\phi[f](x_j), \quad (83)$$

and we call the derivatives of this QMC estimate the empirical derivatives of $\mathcal{H}_\phi[f]$. We are interested in proving the convergence of the empirical gradients of $\mathcal{H}_\phi[f]$ with respect to its input f as well as the parameters ϕ of the layer. As in Appendix B.1, we write $\pi f = \{f(x_j)\}_{j=1}^N$.

Theorem 2 *For any INR-Net layer \mathcal{H}_ϕ which takes an INR $f \in \mathcal{F}_m$ as input, the empirical gradient of $\mathcal{H}_\phi[f]$ w.r.t. its parameters ϕ is convergent in N :*

$$\lim_{N \rightarrow \infty} |\nabla_\phi \hat{H}_\phi^N[f]| < \infty. \quad (84)$$

Additionally, the empirical gradient of $\mathcal{H}_\phi[f]$ w.r.t. its discretized input πf is convergent in N :

$$\lim_{N \rightarrow \infty} |\nabla_{\pi f} \hat{H}_\phi^N[f]| < \infty. \quad (85)$$

Proof:

INR to Vector: gradients w.r.t. parameters Consider the case of a layer $\mathcal{H}_\phi : \mathcal{F}_m \rightarrow \mathbb{R}^n$. As in (1), such a layer can be expressed as:

$$\mathcal{H}_\phi[f] = \int_{\Omega} h(x, f(x), \dots, D^\alpha f(x); \phi) dx, \quad (86)$$

for some h parameterized by ϕ , with weak derivatives up to order $|\alpha|$ taken with respect to each channel.

If $\phi = (\phi_1, \dots, \phi_K)$, then denote $\phi + \tau e_k = (\phi_1, \dots, \phi_{k-1}, \phi_k + \tau, \phi_{k+1}, \dots, \phi_K)$.

$$\lim_{N \rightarrow \infty} \frac{\partial}{\partial \phi_k} \hat{H}_\phi^N[f] = \lim_{N \rightarrow \infty} \frac{\partial}{\partial \phi_k} \left(\frac{1}{N} \sum_{j=1}^N H_\phi[f](x_j) \right) \quad (87)$$

$$= \lim_{N \rightarrow \infty} \lim_{\tau \rightarrow 0} \left(\frac{1}{\tau N} \sum_{j=1}^N H_{\phi + \tau e_k}[f](x_j) - H_\phi[f](x_j) \right) \quad (88)$$

$$= \lim_{\tau \rightarrow 0} \frac{1}{\tau} \int_{\Omega} h(x, f(x), \dots, \phi + \tau e_k) - h(x, f(x), \dots, \phi) dx \quad (89)$$

$$= \lim_{\tau \rightarrow 0} \frac{\mathcal{H}_{\phi + \tau e_k}[f] - \mathcal{H}_\phi[f]}{\tau} \quad (90)$$

$$= \frac{\partial}{\partial \phi_k} \mathcal{H}_\phi[f], \quad (91)$$

where (89) follows by eqn. (86) and the Moore-Osgood theorem. Thus the empirical gradient converges to the Jacobian of \mathcal{H}_ϕ w.r.t. each parameter, which is finite by assumption.

INR to INR: gradients w.r.t. parameters From (3), we stated that an INR-Net layer $\bar{\mathcal{H}}_{\phi'} : L^2(\Omega) \rightarrow L^2(\Omega)$ can be expressed as:

$$\bar{\mathcal{H}}_{\phi'}[f](x') = \int_{\Omega} \bar{h}(x, f(x), \dots, D^\alpha f(x), x', f(x'), \dots, D^\alpha f(x'); \phi') dx. \quad (92)$$

We can in fact follow the same steps as the INR to Vector case above, to arrive at:

$$\lim_{N \rightarrow \infty} \frac{\partial}{\partial \phi'_k} \left(\frac{1}{N} \sum_{j=1}^N \bar{H}_{\phi'}[f] \right) = \frac{\partial}{\partial \phi'_k} \bar{\mathcal{H}}_{\phi'}[f], \quad (93)$$

with equality at each point $x' \in \Omega$ and channel of the output INR.

INR input: gradients w.r.t. inputs Here we combine the INR to vector and INR to INR cases for brevity. For fixed $\tilde{x} \in \Omega$, the empirical derivative of \mathcal{H}_ϕ w.r.t. $f(\tilde{x})$ can be written:

$$\frac{\partial}{\partial f(\tilde{x})} \hat{H}_\phi^N[f] = \frac{\partial}{\partial f(\tilde{x})} \left(\frac{1}{N} \sum_{j=1}^N H_\phi[f](x_j) \right) \quad (94)$$

$$= \lim_{\tau \rightarrow 0} \frac{1}{\tau N} \sum_{j=1}^N H_\phi[f + \tau \psi_{\tilde{x}, N}](x_j) - H_\phi[f](x_j), \quad (95)$$

where $\psi_{\tilde{x}, N}$ is any function in $W^{|\alpha|, 1}(\Omega)$ that is 1 at \tilde{x} and 0 at every $x_j \neq \tilde{x}$, and whose weak derivatives are 0 at every x_j . As an example, take the bump function which vanishes outside a small neighborhood of \tilde{x} and smoothly ramps to 1 on a smaller neighborhood of \tilde{x} , making its weak derivatives 0 at \tilde{x} .

By (8) we know that the sequences $\left\| \hat{H}_\phi^N[f] - \mathcal{H}_\phi[f] \right\|$ and $\left\| \hat{H}_\phi^N[f + \tau \psi_{\tilde{x}, N}] - \mathcal{H}_\phi[f + \tau \psi_{\tilde{x}, N}] \right\|$ converge uniformly in N to 0 for any $\tau > 0$, where we can use the ℓ_1 norm for vector outputs or the L^1 norm for INR outputs. So for any $\epsilon > 0$ and any $\tau > 0$, we can choose N_0 large enough such that for any $N > N_0$:

$$\left\| \hat{H}_\phi^N[f + \tau \psi_{\tilde{x}, N}] - \mathcal{H}_\phi[f + \tau \psi_{\tilde{x}, N}] \right\| < \frac{\epsilon}{2}, \quad (96)$$

and

$$\left\| \hat{H}_\phi^N[f] - \mathcal{H}_\phi[f] \right\| < \frac{\epsilon}{2}. \quad (97)$$

Then,

$$\left\| \hat{H}_\phi^N[f + \tau\psi_{\tilde{x},N}] - \mathcal{H}_\phi[f + \tau\psi_{\tilde{x},N}] \right\| + \left\| \hat{H}_\phi^N[f] - \mathcal{H}_\phi[f] \right\| < \epsilon, \quad (98)$$

by the triangle inequality,

$$\left\| (\hat{H}_\phi^N[f + \tau\psi_{\tilde{x},N}] - \mathcal{H}_\phi[f + \tau\psi_{\tilde{x},N}]) - (\hat{H}_\phi^N[f] - \mathcal{H}_\phi[f]) \right\| < \epsilon \quad (99)$$

$$\left\| (\hat{H}_\phi^N[f + \tau\psi_{\tilde{x},N}] - \hat{H}_\phi^N[f]) - (\mathcal{H}_\phi[f + \tau\psi_{\tilde{x},N}] - \mathcal{H}_\phi[f]) \right\| < \epsilon, \quad (100)$$

hence $\left\| (\hat{H}_\phi^N[f + \tau\psi_{\tilde{x},N}] - \hat{H}_\phi^N[f]) - (\mathcal{H}_\phi[f + \tau\psi_{\tilde{x},N}] - \mathcal{H}_\phi[f]) \right\|$ converges uniformly to 0. Since the distance between two vectors is 0 iff they are the same, we can write:

$$\lim_{N \rightarrow \infty} \hat{H}_\phi^N[f + \tau\psi_{\tilde{x},N}] - \hat{H}_\phi^N[f] = \lim_{N \rightarrow \infty} \mathcal{H}_\phi[f + \tau\psi_{\tilde{x},N}] - \mathcal{H}_\phi[f] \quad (101)$$

$$\lim_{\tau \rightarrow 0} \frac{1}{\tau} \lim_{N \rightarrow \infty} (\hat{H}_\phi^N[f + \tau\psi_{\tilde{x},N}] - \hat{H}_\phi^N[f]) = \lim_{\tau \rightarrow 0} \frac{1}{\tau} \lim_{N \rightarrow \infty} (\mathcal{H}_\phi[f + \tau\psi_{\tilde{x},N}] - \mathcal{H}_\phi[f]). \quad (102)$$

By the Moore-Osgood theorem,

$$\lim_{N \rightarrow \infty} \lim_{\tau \rightarrow 0} \frac{1}{\tau} (\hat{H}_\phi^N[f + \tau\psi_{\tilde{x},N}] - \hat{H}_\phi^N[f]) = \lim_{N \rightarrow \infty} \lim_{\tau \rightarrow 0} \frac{1}{\tau} (\mathcal{H}_\phi[f + \tau\psi_{\tilde{x},N}] - \mathcal{H}_\phi[f]) \quad (103)$$

$$\lim_{N \rightarrow \infty} \frac{\partial}{\partial f(\tilde{x})} \hat{H}_\phi^N[f] = \lim_{N \rightarrow \infty} d\mathcal{H}_\phi[f; \psi_{\tilde{x},N}]. \quad (104)$$

The limit on the right hand side is finite due to Fréchet differentiability of H_ϕ at all f .

Choose a family $\{\Psi_N\}_{N \in \mathbb{N}}$ of decreasing sequences of bump functions around each x_j , $\Psi_N = \{\psi_{x_j, N}\}_{j=1}^N$. An example of such a family is the (appropriately designed) partitions of unity with N elements.

Then the empirical gradient w.r.t. πf converges to the limit of the Gateaux derivatives of \mathcal{H}_ϕ w.r.t. the bump function sequences in this family. \square

Theorem 3 *Chained empirical derivatives converge in N to the chained Gateaux derivatives.*

Proof: Consider a two-layer INR-Net with INR input $f \mapsto (\mathcal{H}_\theta \circ \mathcal{H}_\phi)[f]$. For the case of derivatives w.r.t. the input, we would like to show the analogue of (104):

$$\lim_{N \rightarrow \infty} \frac{\partial}{\partial f(\tilde{x})} (\hat{H}_\theta^N \circ \hat{H}_\phi^N)[f] = \lim_{N \rightarrow \infty} d(\mathcal{H}_\theta \circ \mathcal{H}_\phi)[f; \psi_{\tilde{x},N}], \quad (105)$$

where the bump function $\psi_{\tilde{x},N}$ is defined similarly (1 at \tilde{x} and 0 at each $x_j \neq \tilde{x}$).

$$\frac{\partial}{\partial f(\tilde{x})} (\hat{H}_\theta^N \circ \hat{H}_\phi^N)[f] = \frac{\partial}{\partial f(x)} (H_\theta [\hat{H}_\phi^N[f]](x_j)) \quad (106)$$

$$= \lim_{\tau \rightarrow 0} \frac{1}{\tau} (H_\theta [\hat{H}_\phi^N[f + \tau\psi_{\tilde{x},N}]](x_j) - H_\theta [\hat{H}_\phi^N[f]](x_j)) \quad (107)$$

as in (95).

By (8) we know $\left\| \mathcal{H}_\theta [\hat{H}_\phi^N[f + \tau\psi_{\tilde{x},N}]] - \hat{H}_\theta [\hat{H}_\phi^N[f + \tau\psi_{\tilde{x},N}]] \right\|$ converges to 0 in N for all $\tau > 0$ (where we can use the ℓ_1 norm for vector outputs or the L^1 norm for INR outputs), as does $\left\| \mathcal{H}_\theta [\hat{H}_\phi^N[f]] - \hat{H}_\theta [\hat{H}_\phi^N[f]] \right\|_{L^1}$. Reasoning as in (96)-(103), we have:

$$\lim_{N \rightarrow \infty} \lim_{\tau \rightarrow 0} \frac{1}{\tau} (H_\theta [\hat{H}_\phi^N[f + \tau\psi_{\tilde{x},N}]] - \hat{H}_\theta [\hat{H}_\phi^N[f]]) \quad (108)$$

$$= \lim_{\tau \rightarrow 0} \frac{1}{\tau} \lim_{N \rightarrow \infty} (\mathcal{H}_\theta [\hat{H}_\phi^N[f + \tau\psi_{\tilde{x},N}]] - \mathcal{H}_\theta [\hat{H}_\phi^N[f]]) \quad (109)$$

$$= \lim_{N \rightarrow \infty} \lim_{\tau \rightarrow 0} \frac{1}{\tau} (\mathcal{H}_\theta [\mathcal{H}_\phi^N[f + \tau\psi_{\tilde{x},N}]] - \mathcal{H}_\theta [\mathcal{H}_\phi^N[f]]) \quad (110)$$

Note that

$$d\mathcal{H}[f; \psi_{\bar{x}, N}] = \frac{1}{\tau} (\mathcal{H}_\phi^N[f + \tau\psi_{\bar{x}, N}] - \mathcal{H}_\phi^N[f] + o(\tau)) \quad (111)$$

$$\mathcal{H}_\phi^N[f + \tau\psi_{\bar{x}, N}] = \mathcal{H}_\phi^N[f] + \tau d\mathcal{H}[f; \psi_{\bar{x}, N}] + o(\tau). \quad (112)$$

Then we complete the equality in (105) as follows:

$$\text{LHS} = \lim_{N \rightarrow \infty} \frac{\partial}{\partial f(\bar{x})} \left(\hat{H}_\theta^N \circ \hat{H}_\phi^N \right) [f] \quad (113)$$

$$= \lim_{N \rightarrow \infty} \lim_{\tau \rightarrow 0} \frac{1}{\tau} (\mathcal{H}_\theta [\mathcal{H}_\phi^N[f + \tau\psi_{\bar{x}, N}]] - \mathcal{H}_\theta [\mathcal{H}_\phi^N[f]]) \quad (114)$$

$$= \lim_{N \rightarrow \infty} \lim_{\tau \rightarrow 0} \frac{1}{\tau} (\mathcal{H}_\theta [\mathcal{H}_\phi^N[f] + \tau d\mathcal{H}[f; \psi_{\bar{x}, N}]] - \mathcal{H}_\theta [\mathcal{H}_\phi^N[f]]) \quad (115)$$

$$= \lim_{N \rightarrow \infty} d\mathcal{H}_\theta [\mathcal{H}_\phi[f]; d\mathcal{H}_\phi[f; \psi_{\bar{x}, N}]] \quad (116)$$

$$= \lim_{N \rightarrow \infty} d(\mathcal{H}_\theta \circ \mathcal{H}_\phi) [f; \psi_{\bar{x}, N}] \quad (117)$$

$$= \text{RHS}, \quad (118)$$

by the chain rule for Gateaux derivatives.

The case of derivatives w.r.t. parameters is straightforward. In the same way we used (96)-(103) to obtain (110), we have:

$$\lim_{N \rightarrow \infty} \frac{\partial}{\partial \phi_k} (\hat{H}_\theta^N \circ \hat{H}_\phi^N) [f] = \lim_{N \rightarrow \infty} \lim_{\tau \rightarrow 0} \frac{1}{\tau} \left(\hat{H}_\theta^N [\hat{H}_{\phi+\tau e_k}^N [f]] - \hat{H}_\theta^N [\hat{H}_\phi^N [f]] \right) \quad (119)$$

$$= \lim_{\tau \rightarrow 0} \frac{1}{\tau} (\mathcal{H}_\theta [\mathcal{H}_{\phi+\tau e_k} [f]] - \mathcal{H}_\theta [\mathcal{H}_\phi [f]]) \quad (120)$$

$$= \frac{\partial}{\partial \phi_k} (\mathcal{H}_\theta \circ \mathcal{H}_\phi) [f], \quad (121)$$

Inductively, the chained derivatives extend to an arbitrary number of layers. \square

Since the properties of INR-Net layers extend to loss functions on INR-Nets, we can treat a loss function similarly to a layer, and write:

$$\mathcal{L}_{g'} [g] = \int_{\Omega} L[g, g'](x) dx \quad (122)$$

$$\hat{L}_{g'}^N [g] = \frac{1}{N} \sum_{j=1}^N L[g, g'](x_j) \quad (123)$$

$$\lim_{N \rightarrow \infty} \frac{\partial}{\partial f(\bar{x})} \left(\hat{L}_{g'}^N \circ \hat{H}_\theta^N \circ \hat{H}_\phi^N \right) [f] = \lim_{N \rightarrow \infty} d(\mathcal{L}_{g'} \circ \mathcal{H}_\theta \circ \mathcal{H}_\phi) [f; \psi_{\bar{x}, N}], \quad (124)$$

where g' can be some other input to the loss function such as ground truth labels. Thus, we can state the following result.

Corollary 5 *The gradients of an INR-Net's loss function w.r.t. its inputs and all its parameters are convergent in the number of QMC sample points.*

C INR-Net Layers

We use c_{in} to denote the number of channels of an input INR and c_{out} to denote the number of channels of an output INR.

Convolution layer The convolution layer aggregates information locally and across channels. It has $c_{\text{in}} c_{\text{out}}$ learned filters K_{ij} , which are defined on some support S which may be a ball or orthotope. The layer also learns scalar biases b_j for each output channel:

$$g_j = \sum_{i=1}^{c_{\text{in}}} K_{ij} * f_i + b_j, \quad (125)$$

with $*$ the continuous convolution as in (7).

To replicate the behavior of a discrete convolution layer with odd kernel size, S is zero-centered. For even kernel size, we shift S by half the dimensions of a pixel. We use a 2nd order B-spline for 3×3 filters and 3rd order for larger filters. We use deBoor’s algorithm to evaluate the spline at intermediate points.

Different padding behaviors from the discrete case are treated differently. Zero-padding is replicated by scaling $\mathcal{H}[f](x)$ by $\frac{|(S+x) \cap \Omega|}{S+x}$ where $S+x$ is the kernel support S translated by x . For reflection padding, the value of the INR at points outside its domain are calculated by reflection. For no padding, the INR’s domain is reduced accordingly, dropping all sample points that are no longer on the new domain.

Linear combinations of channels Linear combinations of channels mimic the function of 1×1 convolutional layers in conventional networks. For learned scalar weights W_{ij} and biases b_j :

$$g_j(x) = \sum_{i=1}^{c_{in}} W_{ij} f_i(x) + b_j, \quad (126)$$

for all $x \in \Omega$. These weights and biases can be straightforwardly copied from a 1×1 convolutional layer to obtain the same behavior. One can also adopt a normalized version, sometimes used in attention-based networks:

$$W_{ij} = \frac{w_{ij}}{\sum_{k=1}^{c_{in}} w_{kj}} \quad (127)$$

Normalization All forms of layer normalization readily generalize to the continuous setting by estimating the statistics of each channel with QMC integration, then applying point-wise operations. These layers typically rescale each channel to have some mean m_i and standard deviation s_i .

$$\mu_i = \int_{\Omega} f_i(x) dx \quad (128)$$

$$\sigma_i^2 = \int_{\Omega} f_i(x)^2 dx - \mu_i^2 \quad (129)$$

$$g_i(x) = \frac{f_i(x) - \mu_i}{\sigma_i + \epsilon} \times s_i + m_i, \quad (130)$$

where we assume dx is normalized and $\epsilon > 0$ is a small constant. Just as in the discrete case, μ_i and σ_i^2 can be a moving average of the means and variances observed over the course of training different INRs, and they can also be averaged over a minibatch of INRs (batch normalization) or calculated per datapoint (instance normalization). Mean m_i and standard deviation s_i can be learned directly (batch normalization), conditioned on other data (adaptive instance normalization), or fixed at 0 and 1 respectively (instance normalization).

Max pooling Max pooling is only a well-defined INR-Net layer if each INR channel is in $L^\infty(\Omega)$. Assuming this is the case, there are two natural generalizations of the max pooling layer to a collection of points: 1) assigning each point to the maximum of its k nearest neighbors, and 2) taking the maximum value within a fixed-size window around each point. However, both of these specifications change the output’s behavior as the density of points increases. In the first case, nearest neighbors become closer together so pooling occurs over smaller regions where there is less total variation in the INR. In the second case, the empirical maximum increases monotonically as the INR is sampled more finely within each window. Because we may want to change the number of sampling points on the fly, both of these behaviors are detrimental.

If we consider the role of max pooling as a layer that shuttles gradients through a strong local activation, then it is sufficient to use a fixed-size window with some scaling factor that mitigates the impact of changing the number of sampling points. Consider the following simplistic model: assume each point in a given patch of an INR channel is an i.i.d. sample from $\mathcal{U}([-b, b])$. Then the maximum of N samples $\{f_i(x_j)\}_{j=1}^N$ is on average $\frac{N-1}{N+1}b$. So we can achieve an “unbiased” max pooling layer by taking the maximum value observed in each window and scaling it by $\frac{N+1}{N-1}$ (if $N = 1$ or our

empirical maximum is negative then we simply return the maximum), then (optionally) multiplying a constant to match the discrete layer.

To replicate the behavior of a discrete max pooling layer with even kernel size, we shift the window by half the dimensions of a pixel, just as in the case of convolution.

Tokenization To tokenize an INR, we choose a finite set of non-overlapping regions $\omega_j \subset \Omega$ of equal measure such that $\cup_j \omega_j = \Omega$. We apply the indicator function of each set to each channel f_i . An embedding of each $f_i|_{\omega_j}$ into \mathbb{R}^n can be obtained by taking its inner product with a polynomial function whose basis spans each $L^2(\omega_j)$. To replicate a pre-trained embedding matrix, we interpolate the weights with B-spline surfaces.

Average pooling An average pooling layer performs a continuous convolution with a box filter, followed by downsampling. To reproduce a discrete average pooling with even kernels, the box filter is shifted, similarly to max pooling.

An adaptive average pooling layer can be replicated by tokenizing the INR and taking the mean of each token to produce a vector of the desired size.

Parametric functions in $L^2(\Omega)$ There are several choices of parametric functions in $L^2(\Omega)$. Such functions can enable an INR to be modulated by taking its elementwise product with the function, or for global information to be aggregated in a learned manner by taking its inner product with the function. If Ω is a subset of $[a, b]^d$, one can use a separable basis defined by the product of rescaled 1D Legendre polynomials along each dimension. If Ω is a d -ball, we can use the Zernike polynomial basis. For any Ω , the function can be represented as an MLP.

Attention layer There are various ways to replicate the functionality of an attention layer. Here we present an approach that preserves the domain. For some $d_k \in \mathbb{N}$ consider a self-attention layer with $c_{\text{in}}d_k$ parametric functions $q_{ij} \in L^2(\Omega)$, $c_{\text{in}}d_k$ parametric functions $k_{ij} \in L^2(\Omega)$, and a convolution with d_k output channels, produce the output INR g as:

$$Q_j = \langle q_{ij}, f_i \rangle \quad (131)$$

$$K_j = \langle k_{ij}, f_i \rangle \quad (132)$$

$$V[f] = \sum_{i=1}^{c_{\text{in}}} v_{ij} * f_i + b_j \quad (133)$$

$$g(x) = \text{softmax} \left(\frac{QK^T}{\sqrt{d_k}} \right) V[f](x) \quad (134)$$

A cross-attention layer generates queries from a second input INR. A multihead-attention layer generates several sets of (Q, K, V) triplets and takes the softmax of each set separately.

Activation Layer Pointwise nonlinearities are identical to the discrete case. We use rectified linear units (ReLU) for all our models.

Positional encoding Adding positional encodings is performed similarly to the discrete case, adding a sinusoidal function of the coordinates to each channel.

Dropout layer Beyond the classic dropout layer which randomly set points and/or channels to zero, there is potential for a dropout layer that reduces computation by randomly dropping QMC sample points or skipping their evaluation under the integral.

Data augmentation Most data augmentation techniques, including spatial transformations, point-wise functions and normalizations, translate naturally to INRs. Furthermore, spatial transformations are efficient and do not incur the usual cost of interpolating back to the grid. This suggests that INR-Nets may benefit from new data augmentation methods such as adding Gaussian noise to the coordinates of QMC sample points.



Figure D.1: Comparison of SIREN (left) and Gaussian Fourier feature network (right) representations of an image, rendered at 256×256 resolution. The Fourier feature network’s representation is slightly blurrier (compare the tree bark), but this effect is not noticeable at lower resolutions.

D Implicit Neural Datasets

D.1 ImageNet INRs

We split ImageNet1k into 12 superclasses (dog, structure/construction, bird, clothing, wheeled vehicle, reptile, carnivore, insect, musical instrument, food, furniture, primate) based on the `big_12` dataset [14], which is in turn derived from the WordNet hierarchy.

We fit SIREN [37] to each image in ImageNet using 5 fully connected layers with 256 channels and sine non-linearities, trained for 2000 steps with an Adam optimizer at a learning rate of 10^{-4} . It takes coordinates on $[-1, 1]^2$ and produces RGB values in $[-1, 1]^3$. We fit Gaussian Fourier feature [41] networks using 4 fully connected layers with 256 channels with ReLU activations. It takes coordinates on $[0, 1]^2$ and produces RGB values in $[0, 1]^3$.

The average pixel-wise error of SIREN is $3 \cdot 10^{-4} \pm 2 \cdot 10^{-4}$, compared to $1.6 \cdot 10^{-2} \pm 8 \cdot 10^{-3}$ for Gaussian Fourier feature networks. The difference in quality is visible at high resolution, but indistinguishable at low resolution (Fig. D.1).

INR-Net-2 uses strided MLP convolutions, a global average pooling layer, then two fully connected layers. INR-Net-4 adds a residual block with two MLP convolutions after the strided convolutions.

D.2 Cityscapes INRs

SIREN is trained on Cityscapes images for 2500 steps, using the same architecture and settings as ImageNet. The average pixel-wise error is $3.6 \cdot 10^{-4} \pm 1.8 \cdot 10^{-4}$.

INR-Net-3 uses three MLP convolutional layers at the same resolution. INR-Net-5 uses a strided MLP convolution to perform downsampling and nearest neighbor interpolation for upsampling. There is a residual connection between the higher resolution layers.

E Additional Analysis

E.1 Using INR-Net with high-discrepancy sequences

If discrepancy were the primary driver of performance, then one might expect the most effective sampling scheme to have the lowest discrepancy at test time, regardless of the sampling scheme used at training time. However, we instead find that the performance of INR-Net is highest when the sampling schemes are consistent between training and evaluation (Table E.1). We observe this pattern for INR classifiers trained with each of three sampling schemes (QMC, Grid, and Shrunk). Switching to a lower discrepancy sampling scheme at test time can degrade performance, sometimes

Table E.1: Performance of INR-Net classifier under various sampling sequences for estimating integrals.

Train→Test Type	Accuracy
QMC→Grid	53.7%
Grid→QMC	54.4%
QMC→Shrunk	51.3%
Shrunk→QMC	33.9%
Grid→Grid	55.8%
QMC→QMC	56.6%
Shrunk→Shrunk	57.0%

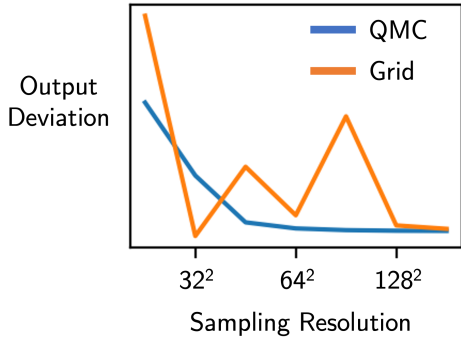


Figure E.1: Distance of the output of a INR-Net from its grid output at 32×32 resolution, when sampling at various resolutions.

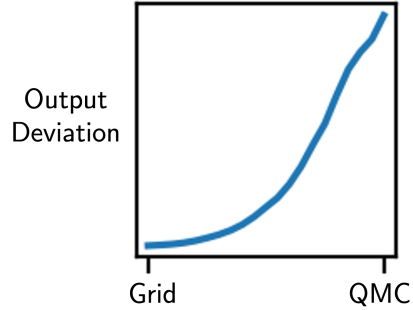


Figure E.2: An INR-Net’s output diverges as sample points are gradually shifted from a grid layout to a low discrepancy sequence.

quite severely (see Shrunk→QMC). A “Shrunk” sampling scheme is one where we shrink a low discrepancy point set towards the center of the image (each coordinate $x_j \in [-1, 1]^2$ becomes $x_j^2 \text{sgn}(x_j)$). In image classification, the object of interest is often centered in the image, which may explain why the shrunk sequence performs slightly better than QMC.

We also find that the output of an INR-Net is less stable under changing sampling resolution with a grid pattern (Fig. E.1). While the output of a network with QMC sampling converges at high resolution, the grid sampling scheme has unstable outputs until very high resolution. Only the grids that overlap each other (resolutions in powers of two) produce similar activations.

E.2 Initialization with discrete networks

Figure E.2 illustrates that the behavior of a pre-trained INR-Net is not preserved when its sampling scheme switches to QMC. For a INR-Net initialized with a truncated EfficientNet, its outputs deviate rapidly as points shift from a regular grid to a low discrepancy sequence.

In Table E.2 and E.3, we illustrate that INR-Net initialized with a large pre-trained discrete network does not match the performance of the original model when fine-tuned with QMC sampling. We use a truncated version of EfficientNet [39] for classification, and fine-tune for 200 samples per class. For segmentation we use a truncated version of ConvNexT-UPerNet [21], fine-tuning with 1000 samples.

Our preliminary experience with INR-Nets highlights the need for improved sampling schemes and parameterizations that will allow large continuous-domain neural networks to learn effectively. Stable, scalable methods are needed to realize INR-Nets’ full potential for continuous data analysis.

Table E.2: Pre-trained models fine-tuned on ImageNet INR classification.

Model Type	Accuracy
EfficientNet [39]	66.4%
INR-Net-EN	48.1%

Table E.3: Pre-trained models fine-tuned on Cityscapes segmentation.

Model Type	Mean IoU	Pixel Accuracy
ConvNexT [21]	0.429	68.1%
INR-Net-CN	0.376	68.7%